Communications in Nonlinear Science and Numerical Simulation 110 (2022) 106372

Contents lists available at ScienceDirect

Communications in Nonlinear Science and Numerical Simulation

journal homepage: www.elsevier.com/locate/cnsns

Research paper

Euler integral as a source of chaos in the three–body problem

Sara Di Ruzza *, Gabriella Pinzari

Dipartimento di Matematica Tullio Levi-Civita, Università degli Studi di Padova, Via Trieste 63, 35121 Padova, Italy

ARTICLE INFO

Article history:
Received 9 September 2021
Received in revised form 29 January 2022
Accepted 21 February 2022
Available online 16 March 2022

Keywords:
Three-body problem
Euler integral
Symbolic dynamics

ABSTRACT

In this paper we address, from a purely numerical point of view, the question, raised in Pinzari (2019), Pinzari (2020), and partly considered in Pinzari (2020), Di Ruzza et al. (2020), Chen and Pinzari (2021), whether a certain function, referred to as "Euler Integral", is a quasi-integral along the trajectories of the three-body problem. Differently from our previous investigations, here we focus on the region of the "unperturbed separatrix", which turns to be complicated by a collision singularity. Concretely, we reduce the Hamiltonian to two degrees of freedom and, after fixing some energy level, we discuss in detail the resulting three-dimensional phase space around an elliptic and an hyperbolic periodic orbit. After measuring the strength of variation of the Euler Integral (which are in fact small), we detect the existence of chaos closely to the unperturbed separatrix. The latter result is obtained through a careful use of the machinery of covering relations, developed in Gierzkiewicz and Zgliczyński (2019), Zgliczynski and Gidea (2004), Wilczak and Zgliczynski (2003).

1. Purpose of the paper

This paper is a numerical study on the three-body problem. It is to be specified that we deal with (a suitably simplified version of) the Hamiltonian of the *full* three-body problem, where "full" is used here as opposed to the so-called "restricted" problem – maybe more known to non specialists – to which much of the arguments discussed here also can also be applied. The full three-body (in general, many-body) problem inherits much of its reputation – especially in Hamiltonian mechanics – after the breakthrough paper by V. I. Arnold [1] which will be recalled below. In fact, this paper is motivated by previous research [2–5], which here we briefly recall, in order to keep the paper self-contained.

We fix a reference frame $(\mathbf{i}, \mathbf{j}, \mathbf{k})$ in the Euclidean space, which we identify with $\mathbb{R}^3$. In such a space we consider three masses 1, μ and κ, with $\mu, \kappa < 1$, interacting through gravity only. We reduce the translation symmetry relating the positions of two (out of three) masses to the position of the third one, as described in [6, §5]. Contrarily to the usual practice, we choose μ as reference mass (usually, the unit mass is chosen). With such choice, the Hamiltonian governing the motions of the masses 1 and κ is

$$\mathrm{H}_{3\mathrm{b}}(\mathbf{y}', \mathbf{y}, \mathbf{x}', \mathbf{x}) = \frac{\kappa+\mu}{\kappa\mu}\frac{\|\mathbf{y}\|^2}{2} - \frac{\kappa\mu}{\|\mathbf{x}\|} + \frac{\mu+1}{\mu}\frac{\|\mathbf{y}'\|^2}{2} - \frac{\mu}{\|\mathbf{x}'\|} - \frac{\kappa}{\|\mathbf{x}-\mathbf{x}'\|} + \frac{1}{\mu}\mathbf{y}\cdot\mathbf{y}' \,.$$

where $\mathbf{x}' = (x_1', x_2', x_3')$, $\mathbf{x} = (x_1, x_2, x_3)$ are the position coordinates of 1 and k; $\mathbf{y}' = (y_1', y_2', y_3')$, $\mathbf{y} = (y_1, y_2, y_3)$ are their respective linear momenta; $\|\cdot\|$ denotes the Euclidean distance and, finally, the gravity constant has been conventionally fixed to one.

* Corresponding author.
E-mail addresses: sara.diruzza@math.unipd.it (S. Di Ruzza), gabriella.pinzari@math.unipd.it (G. Pinzari).

https://doi.org/10.1016/j.cnsns.2022.106372

The rescaling

$$(\mathbf{y}', \mathbf{y}) \to \frac{\mu^2\kappa^2}{\kappa+\mu}(\mathbf{y}', \mathbf{y}), \qquad (\mathbf{x}', \mathbf{x}) \to \frac{\kappa+\mu}{\mu^2\kappa^2}(\mathbf{x}', \mathbf{x}), \qquad t \to \frac{\mu^3\kappa^3}{\kappa+\mu}t$$

(with t denoting the time) does not alter the motion equations, provided that $\mathrm{H}_{3\mathrm{b}}$ is changed to

$$\mathrm{H}_{3\mathrm{b}}(\mathbf{y}', \mathbf{y}, \mathbf{x}', \mathbf{x}) = \frac{\|\mathbf{y}\|^2}{2} - \frac{1}{\|\mathbf{x}\|} + \delta\left(\frac{\|\mathbf{y}'\|^2}{2} - \frac{\alpha}{\|\mathbf{x}-\mathbf{x}'\|} - \frac{\beta}{\|\mathbf{x}'\|} + \gamma\,\mathbf{y}\cdot\mathbf{y}'\right), \tag{1}$$

with

$$\alpha := \frac{\kappa+\mu}{\kappa\mu(\mu+1)}, \qquad \beta := \frac{\kappa+\mu}{\kappa^2(\mu+1)}, \qquad \gamma := \frac{1}{\mu+1}, \qquad \delta := \frac{\kappa(\mu+1)}{\kappa+\mu}. \tag{2}$$

As only two parameters among (2) can be regarded as independent, from this point on, we choose α and β. This will simplify later analysis (compare Eq. (10) below). We restrict our attention to the so called "planar problem", which corresponds to take the respective third components of position and momentum coordinates identically vanishing: $x_3 = x_3' = y_3 = y_3' = 0$. In such a case, $\mathrm{H}_{3\mathrm{b}}$ in (1) has four degrees of freedom. We now describe a procedure which will reduce the number of degrees of freedom to *two*. One degree of freedom can be eliminated exploiting the "rotations invariance", namely the fact that the Hamiltonian $\mathrm{H}_{3\mathrm{b}}$ remain unchanged under the group of transformations

$$(\mathbf{y}', \mathbf{y}) \to (\mathcal{R}\mathbf{y}', \mathcal{R}\mathbf{y}) \qquad (\mathbf{x}', \mathbf{x}) \to (\mathcal{R}\mathbf{x}', \mathcal{R}\mathbf{x}) \tag{3}$$

where $\mathcal{R}$ is any constant orthogonal matrix, i.e, verifying

$$\mathcal{R}\mathcal{R}^{\mathrm{t}} = \mathrm{I} = \mathcal{R}^{\mathrm{t}}\mathcal{R}$$

with the superscript "t" denoting transpose, and I being the identity matrix. The existence of such group of diffeomorphisms is caused by the conservation of the components of the "angular momentum" vector $\mathbf{C} = (\mathrm{C}_1, \mathrm{C}_2, \mathrm{C}_3)$ given by

$$\mathbf{C} = \mathbf{x}\times\mathbf{y} + \mathbf{x}'\times\mathbf{y}'$$

along the trajectories of $\mathrm{H}_{3\mathrm{b}}$. Clearly, rotation invariance is not specific of the planar problem. In the planar case, it allows for the reduction of one[1] degree of freedom, as $\mathbf{C}$ has one only non-trivial coordinate C_3, which, from now on, we shall simply denote as C. One further degree of freedom can be eliminated under the assumption that the "Keplerian term" outside parentheses in (1), namely,

$$\frac{\|\mathbf{y}\|^2}{2} - \frac{1}{\|\mathbf{x}\|} \tag{4}$$

takes negative values and is "leading" in the Hamiltonian (1). To better specify this assumption, we need to describe canonical coordinates explicitly performing the reduction of (3) and, simultaneously, integrating (4). For the planar case, such coordinates are easy to be produced. We proceed as follows.

On a 6-dimensional "rotation-reduced phase space" (that will be more precisely described in the next Section 2) we fix coordinates

$$(\mathrm{R}, \mathrm{G}, \Lambda, \mathrm{r}, \mathrm{g}, \ell) \tag{5}$$

which equip such space with the two-form

$$\omega = d\mathrm{R}\wedge d\mathrm{r} + d\mathrm{G}\wedge d\mathrm{g} + d\Lambda\wedge d\ell\,.$$

To define the coordinates (5), we note that, as long as the Hamiltonian (4) keeps to be negative, it generates motions on ellipses. We denote as $\mathbb{E}$ the ellipse generated by Hamiltonian (4) for a given initial datum $(\mathbf{y}, \mathbf{x})$. Assuming $\mathbb{E}$ is not a circle, we let

- R is the "radial velocity" of $\mathbf{x}'$; i.e., the projection of the velocity $\mathbf{y}'$ along the direction of $\mathbf{x}'$;
- G is the Euclidean length of the angular momentum $\mathbf{G} = \mathbf{x}\times\mathbf{y}$ of $\mathbf{x}$;
- $\Lambda = \sqrt{a}$, where a is the semi-major axis of $\mathbb{E}$;
- r is the Euclidean length of $\mathbf{x}'$;
- g the angle detecting the perihelion of $\mathbb{E}$;
- ℓ the "mean anomaly of $\mathbf{x}$".

[1] Incidentally, in the general case, the number of degrees of freedom is lowered by *two* units, due to the fact that the components of $\mathbf{C}$ are not pairwise commuting. See [7] for a case study.

Precise formulae will be given below: compare Eq. (23). Here we only mention that, in a sense, the coordinates above are referred to a frame "moving with $\mathbf{x}'$", in order to obtain reduction of rotations. Using the coordinates above, and splitting the term inside parentheses in (1) as the sum of its ℓ-average (denoted as $\overline{\mathrm{H}}_{\mathrm{C}}$) and the zero-average part (denoted as $\widetilde{\mathrm{H}}_{\mathrm{C}}$), we arrive at

$$\mathrm{H}_{3\mathrm{b,C}}(\mathrm{R},\mathrm{G},\Lambda,\mathrm{r},\mathrm{g},\ell)=-\frac{1}{2\Lambda^2}+\delta\Big(\overline{\mathrm{H}}_{\mathrm{C}}(\mathrm{R},\mathrm{G},\Lambda,\mathrm{r},\mathrm{g})+\widetilde{\mathrm{H}}_{\mathrm{C}}(\mathrm{R},\mathrm{G},\Lambda,\mathrm{r},\mathrm{g},\ell)\Big)\,. \tag{6}$$

In the notation, we have remarked that, as an effect of the reduction, the system depends parametrically on the total angular momentum $\mathrm{C}=\|\mathbf{C}\|$.

The Hamiltonian (6) has an involved aspect. By no means it appears as – or can be conjugated to – a standard *close-to-be-integrable system*. These are systems of the form

$$\mathrm{H}(\mathrm{I},\varphi)=\mathrm{h}(\mathrm{I})+\mu f(\mathrm{I},\varphi)$$

where μ is a very small parameter; $(\mathrm{I},\varphi)=(\mathrm{I}_1,\dots,\mathrm{I}_n,\varphi_1,\dots,\varphi_n)$ are coordinates – usually named *action-angle* – taking values in $V\times\mathbb{T}^n$, with $V\subset\mathbb{R}^n$ open and connected and $\mathbb{T}=\mathbb{R}/(2\pi\mathbb{Z})$. We then recover such lack of structure by assigning to each term in (6) a "relative weight". We make two main assumptions. The former is that the Keplerian term (4) is much greater than the zero-average terms

$$\left\|-\frac{1}{2\Lambda^2}\right\|\gg\delta\,\|\widetilde{\mathrm{H}}_{\mathrm{C}}\| \tag{7}$$

where $\|\cdot\|$ is some norm on functions. Under condition (7), and provided that all the functions have a holomorphic extension on some small complex domain, perturbation theory (see [1]) allows us to conjugate the Hamiltonian (6) to

$$\mathrm{H}_{3\mathrm{b,C}}(\mathrm{R},\mathrm{G},\Lambda,\mathrm{r},\mathrm{g},\ell)=-\frac{1}{2\Lambda^2}+\delta\overline{\mathrm{H}}_{\mathrm{C}}(\mathrm{R},\mathrm{G},\Lambda,\mathrm{r},\mathrm{g})+\mathrm{O}_2(\mathrm{R},\mathrm{G},\Lambda,\mathrm{r},\mathrm{g},\ell) \tag{8}$$

where O_2 denotes a remainder term, depending on all coordinates. Let us look at the system which is obtained when the remainder is neglected: for such a system, the first term in (6) becomes an inessential additive term for the averaged Hamiltonian which, without loss of generality (see next Section 2 for a discussion), we fix at

$$\Lambda=1\,. \tag{9}$$

Reabsorbing the parameter δ through a change of time, we are reduced to study the 2-degrees of freedom Hamiltonian $\overline{\mathrm{H}}_{\mathrm{C}}$, which is given by

$$\overline{\mathrm{H}}_{\mathrm{C}}(\mathrm{R},\mathrm{G},\mathrm{r},\mathrm{g})=\frac{\mathrm{R}^2}{2}+\frac{(\mathrm{C}-\mathrm{G})^2}{2\mathrm{r}^2}-\alpha\mathrm{U}(\mathrm{r},\mathrm{G},\mathrm{g})-\frac{\beta}{\mathrm{r}} \tag{10}$$

where we have assumed

$$\mathbf{G}\parallel\mathbf{C}\parallel(\mathbf{C}-\mathbf{G})\parallel\mathbf{k} \tag{11}$$

so that $\|\mathbf{x}'\times\mathbf{y}'\|=\|\mathbf{C}-\mathbf{G}\|=\mathrm{C}-\mathrm{G}$, and we have denoted as

$$\mathrm{U}(\mathrm{r},\mathrm{G},\mathrm{g}):=\frac{1}{2\pi}\int_0^{2\pi}\frac{d\ell}{\|\mathbf{x}'-\mathbf{x}\|} \tag{12}$$

the simply ℓ-averaged[2] of the Newtonian[3] potential (obviously, written using the above coordinates), which turns to be C-independent (see formulae (25) below).

In order to describe the motions we are looking for, we rewrite $\overline{\mathrm{H}}_{\mathrm{C}}$ as

$$\overline{\mathrm{H}}_{\mathrm{C}}=\mathrm{K}_{\mathrm{C}}(\mathrm{R},\mathrm{r})-\alpha\mathrm{U}(\mathrm{r},\mathrm{G},\mathrm{g})+\widetilde{\mathrm{K}}_{\mathrm{C}}(\mathrm{G},\mathrm{r}) \tag{13}$$

where

$$\mathrm{K}_{\mathrm{C}}(\mathrm{R},\mathrm{r})=\frac{\mathrm{R}^2}{2}+\frac{\mathrm{C}^2}{2\mathrm{r}^2}-\frac{\beta}{\mathrm{r}}\,,\quad\widetilde{\mathrm{K}}_{\mathrm{C}}(\mathrm{G},\mathrm{r})=\frac{\mathrm{G}^2-2\mathrm{CG}}{2\mathrm{r}^2}\,.$$

We look at regions of phase space where

$$\|\mathrm{K}_{\mathrm{C}}\|\gg\alpha\|\mathrm{U}\|\gg\|\widetilde{\mathrm{K}}_{\mathrm{C}}\|\,. \tag{14}$$

which is our second assumption.

[2] Here, "simply" is used as opposed to the more familiar "doubly" averaged Newtonian potential, most often encountered in the literature; e.g. [1,7–11].

[3] We call "Newtonian potential" the function $\frac{1}{\|\mathbf{x}-\mathbf{x}'\|}$. Note that the term $\gamma\mathbf{y}'\cdot\mathbf{y}$ has zero-average (being $\mathbf{y}$ proportional to the ℓ-derivative of $\mathbf{x}$ and $\mathbf{y}'$ ℓ-independent), so it is merged in $\widetilde{\mathrm{H}}_{\mathrm{C}}$, together with the zero-average part $\widetilde{\mathrm{U}}$ of the Newtonian potential.

Let us briefly comment on inequalities (7) and (14). These inequalities aim to shape the Hamiltonian (8) as a *three-scales* system, namely, composed, at a first order of approximation, of three simpler terms of very different sizes. In particular, under such inequalities, one may argue that, at a first order of approximation, the motions $(\Lambda(t), \mathrm{R}(t), \mathrm{G}(t), \ell(t), \mathrm{r}(t), \mathrm{g}(t))$ of $\mathrm{H}_{3\mathrm{b,C}}$ are as follows:

Conjecture 1.1.

- $\Lambda(t) \sim 1$ *remains almost constant and* $\ell(t) \sim t$ *moves fast;*
- *the motion* $(\mathrm{R}(t), \mathrm{r}(t))$ *is ruled by* $\mathrm{K_C}$*;*
- *the motion* $(\mathrm{G}(t), \mathrm{g}(t))$ *is ruled by the non-autonomous Hamiltonian* $\mathrm{U}(\mathrm{r}(t), \cdot, \cdot)$. □

Now, the term $\mathrm{K_C}$ is well-known. It consists of the one degree of freedom reduction of a Hamiltonian as in (4), with a fictitious angular momentum equal to C. The coordinate r moves as the length of a vector along a conic section (which can be an ellipse, parabola or hyperbola, according to the sign of the energy $\mathrm{K_C}$) according to the Law of Equal Areas. To understand the dynamics generated by $\mathrm{U}(\mathrm{r}, \cdot, \cdot)$, we need to recall a property of such a function, pointed out in [2]. First of all, we remark that U is integrable. But the main point is that there exists a function F of two arguments such that

$$\mathrm{U}(\mathrm{r}, \mathrm{G}, \mathrm{g}) = \mathrm{F}(\mathrm{r}, \mathrm{E}(\mathrm{r}, \mathrm{G}, \mathrm{g})) \tag{15}$$

where

$$\mathrm{E}(\mathrm{r}, \mathrm{G}, \mathrm{g}) = \mathrm{G}^2 - \mathrm{r}\sqrt{1-\mathrm{G}^2}\cos\mathrm{g}\,. \tag{16}$$

The function $\mathrm{E}(\mathrm{r}, \mathrm{G}, \mathrm{g})$ above will be referred to as *Euler integral*, as it appears in the integration of the two-fixed centres Hamiltonian (also known as *Euler problem*). By (15), the level sets of E, namely the curves

$$\mathcal{S}(\mathrm{r}, \mathcal{E}) := \left\{(\mathrm{G}, \mathrm{g}): \quad \mathrm{G}^2 - \mathrm{r}\sqrt{1-\mathrm{G}^2}\cos\mathrm{g} = \mathcal{E}\right\} \tag{17}$$

are also level sets of U. On the other hand, the phase portrait of E can be studied exactly, and this has been done in [5]. We report the main results here. We fix a reference frame with g on the first axis, G on the second one. For the coordinates (g, G), by the periodicity of g, we consider a domain given by the rectangle $[0, 2\pi) \times (-1, 1)$. Then we have three cases.

(a) $0 < \mathrm{r} < 1$. The point $(0, 0)$ is a minimum, while there are two symmetric maxima at $\left(\pi, \pm\sqrt{1-\frac{\mathrm{r}^2}{4}}\right)$ and one saddle at $(\pi, 0)$. The phase portrait includes two separatrices

$$\begin{cases} \mathcal{S}_0(\mathrm{r}) = \{(\mathrm{G}, \mathrm{g}): \ \mathrm{E}(\mathrm{r}, \mathrm{G}, \mathrm{g}) = \mathrm{r}\} \\ \\ \mathcal{S}_1(\mathrm{r}) = \{(\mathrm{G}, \mathrm{g}): \ \mathrm{E}(\mathrm{r}, \mathrm{G}, \mathrm{g}) = 1\} \end{cases} \tag{18}$$

with $\mathcal{S}_0(\mathrm{r})$ going through the saddle $(\pi, 0)$ and $\mathcal{S}_1(\mathrm{r})$ through $(\frac{\pi}{2}, \pm 1)$. Rotational motions in between $\mathcal{S}_0(\mathrm{r})$ and $\mathcal{S}_1(\mathrm{r})$ do exist. $\mathcal{S}_0(\mathrm{r})$ delimits librations about the minimum and rotations. $\mathcal{S}_1(\mathrm{r})$ delimits different librations surrounding the maxima and the saddle and librational motions about the minimum.

(b) $1 < \mathrm{r} < 2$. The minimum $(0, 0)$ persists, as well as the two symmetric maxima $\left(\pi, \pm\sqrt{1-\frac{\mathrm{r}^2}{4}}\right)$, the saddle at $(\pi, 0)$ and the separatrices (18), with the difference, now, that $\mathcal{S}_1(\mathrm{r})$ is inner with respect to $\mathcal{S}_0(\mathrm{r})$, when looking from the minima. Rotational motions disappear, as in fact $\mathcal{S}_0(\mathrm{r})$ delimits librations about the maxima and librations surrounding the maxima and the saddle, while $\mathcal{S}_1(\mathrm{r})$ delimits different librations surrounding the maxima and the saddle and librational motions about the minimum.

(c) $\mathrm{r} > 2$. The saddle point and the separatrix $\mathcal{S}_0(\mathrm{r})$ disappear, as and $(\pi, 0)$ turns to be a maximum, while $(\pi, 0)$ is still a minimum. The phase portrait includes only the separatrix $\mathcal{S}_1(\mathrm{r})$ in (18), which delimits different librational motions about the minimum or the maximum.

The situation is represented in Fig. 2.

It is to be remarked, however, that the coordinate r stays fixed under E, while it moves under $\overline{\mathrm{H}}_\mathrm{C}$. Therefore, three-dimensional plots representing the manifolds corresponding to the "lifted level sets"

$$\mathcal{M}(\mathcal{E}) = \{(\mathrm{r}, \mathrm{G}, \mathrm{g}): \ \mathrm{E}(\mathrm{r}, \mathrm{G}, \mathrm{g}) = \mathcal{E}\} \tag{19}$$

Such manifolds are represented in Fig. 3.

Each manifold $\mathcal{M}(\mathcal{E})$ with $0 < \mathcal{E} < 2$ has a saddle at

$$(\mathrm{r}_{\mathrm{sad}}, \mathrm{G}_{\mathrm{sad}}, \mathrm{g}_{\mathrm{sad}}) = (\mathcal{E}, 0, \pi) \qquad \forall\ 0 < \mathcal{E} < 2\,. \tag{20}$$

The manifolds obtained "lifting" along the r-direction the curves $\mathcal{S}_0(\mathrm{r})$, $\mathcal{S}_1(\mathrm{r})$ in (18) will be denoted as

$$\begin{cases} \mathcal{M}_0 = \{(\mathrm{r}, \mathrm{G}, \mathrm{g}): \ \mathrm{E}(\mathrm{r}, \mathrm{G}, \mathrm{g}) = \mathrm{r}\} \\ \\ \mathcal{M}_1 = \{(\mathrm{r}, \mathrm{G}, \mathrm{g}): \ \mathrm{E}(\mathrm{r}, \mathrm{G}, \mathrm{g}) = 1\} \end{cases}. \tag{21}$$

See Fig. 4.

Combining the phase portraits above with Conjecture 1.1, we pose the following

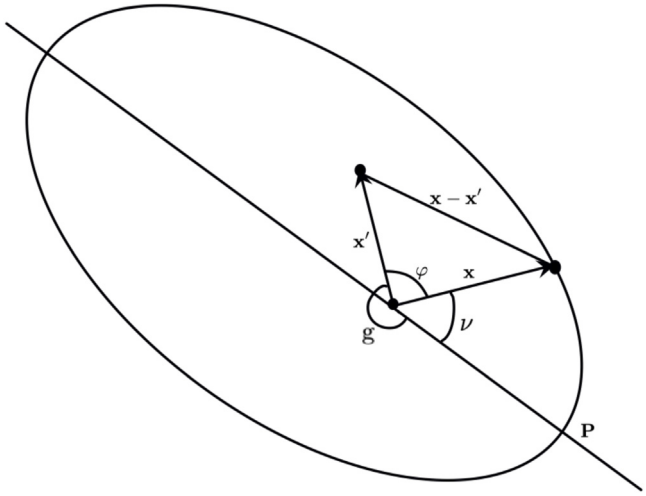

Fig. 1. The three-body problem.

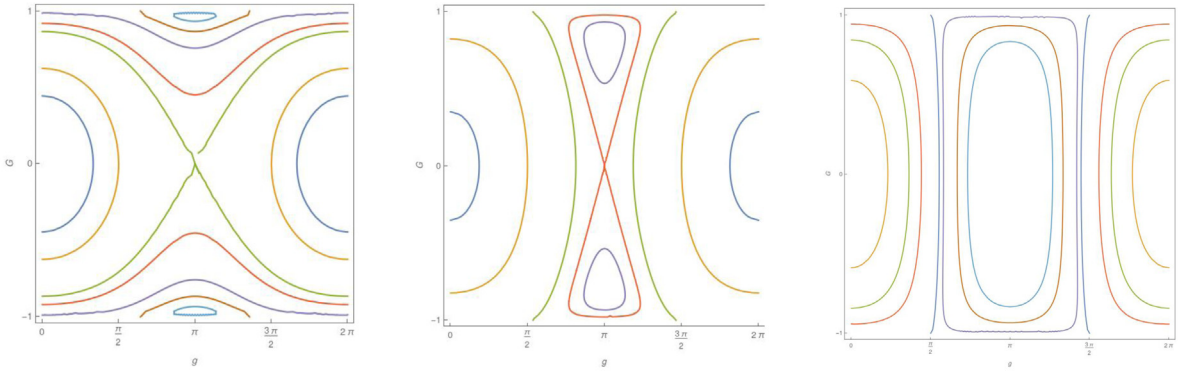

(a) $0 < r < 1$ (b) $1 < r < 2$ (c) $r > 2$

Fig. 2. Sections, at r fixed, of the level surfaces of E.

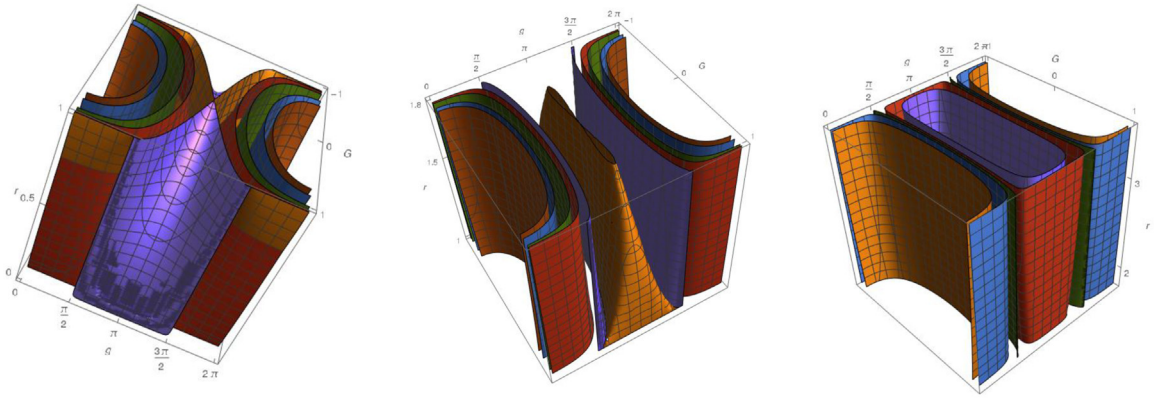

(a) $0 < r < 1$ (b) $1 < r < 2$ (c) $r > 2$

Fig. 3. Logs of the level surfaces of E in the space (r, g, G).

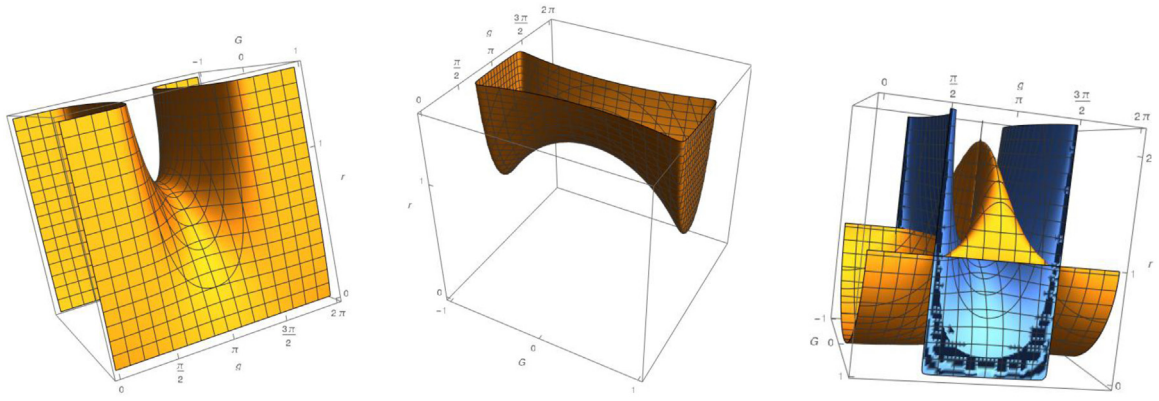

(a) $0 < \mathcal{E} < 1$ (b) $1 < \mathcal{E} < 2$ (c)

Fig. 4. (a) and (b): The saddle point of $\mathcal{M}(\mathcal{E})$; (c): $\mathcal{M}_0$ (yellow) and $\mathcal{M}_1$ (blue).

Conjecture 1.2. *For a set of parameters and in a region of phase space where conditions (7), (14) are verified,*

(i) the manifolds $\mathcal{M}(\mathcal{E})$ are "approximate invariant manifolds" for the Hamiltonian $\mathrm{H}_{3\mathrm{b,C}}$ in (6), at least for the time that r *does not leave a fixed region (a), (b), (c) above;*

(ii) the coupling between K_C and U*, the presence of the "disturbing term" $\widetilde{\mathrm{K}}_\mathrm{C}$ and the remainder O_2 in (8) are source of chaotic dynamics for $\mathrm{H}_{3\mathrm{b,C}}$ in (6), closely to $\mathcal{M}_0$.* □

However, our numerical explorations will only support the following assertion.

Conjecture 1.3. *For a set of parameters and in a region of phase space where condition (14) is verified,*

(i)' the manifolds $\mathcal{M}(\mathcal{E})$ are "approximate invariant manifolds" for the Hamiltonian $\overline{\mathrm{H}}_\mathrm{C}$ in (10), at least for the time that r *does not leave a fixed region (a), (b), (c) above;*

(ii)' the coupling between K_C and U *and the presence of the "disturbing term" $\widetilde{\mathrm{K}}_\mathrm{C}$ are source of chaotic dynamics for $\overline{\mathrm{H}}_\mathrm{C}$ in (10), closely to $\mathcal{M}_0$.* □

Note that Conjecture 1.3 is based on (14), but does not need (7). This is precisely the reason that led us to relax Conjecture 1.2 to the form 1.3. Let us briefly comment on this.

A typical difficulty in Celestial Mechanics is represented by the *lack of parameters*. A famous example goes back to V. I. Arnold, who, in the paper [1], wanted to regard the $(1+n)$-body problem (in the planetary[4] version) as close to n *independent* Kepler Hamiltonians (4). He had at his disposal only *one* parameter, given by the maximum ratio μ of the planets' masses to the sun's. In a very similar situation as for the Hamiltonian (6), where the Keplerian approximation provides motions for only the $(\Lambda, \ell)'$s coordinates, using a *two-scale* approximation (a scale "of order 1" for the motions of the ℓ'*s*; a scale "of order μ" for the motions of the ellipses), he ingeniously found a good approximation for the motions of *all* coordinates. To fulfil[5] this, he required, besides the smallness of the parameter μ, an additive condition (i.e., the smallness of eccentricities and inclinations of the planets' instantaneous ellipses of the planets) having the rôle of pushing away, in the Hamiltonian, remainder terms from the two leading scales terms. Now, inequalities (7) and (14) have the precise scope of emulating Arnold's strategy, with the difference that, in our case, they provide a *three-scale* system. In particular, (7) stresses that the velocity of ℓ is much larger than the velocities of (R, r) and (G, g), in turn separated by (14). Of course, the Hamiltonian $\overline{\mathrm{H}}_\mathrm{C}$ has a physical meaning only whenever (7) is satisfied. However, what is, if existing, a "natural" choice of parameter masses and/or of additive conditions that make (7)–(14) true does not seem immediate to us. For this reason, we choose to investigate the motions of $\overline{\mathrm{H}}_\mathrm{C}$ independently whether condition (7) is verified or not. Our interest in $\overline{\mathrm{H}}_\mathrm{C}$ is indeed precisely related to the Euler integral (16): we aim to find zones in the phase space of $\overline{\mathrm{H}}_\mathrm{C}$ where E affords slow variations and, simultaneously, chaos is detected. A similar point of view has been taken up, on the other hand, in the published papers [3,4,12].

Before switching to technical parts, we recall related works, with no aim of completeness. Chaos in many-body systems has been widely studied in the literature [13–18]. For general information on chaotic phenomena, the reader may consult [19–21]. Closely related papers to the current one are the aforementioned [3,4,12]. Specifically, in [4] Conjecture 1.3 has been proved in the case (c), while in [12] it has been proved in the case (a), with $\mathrm{r} \ll 1$ and for motions very close to

[4] The planetary $(1+n)$-body problem consists of the Newtonian attraction of $1+n$ masses $m_0, \ldots, m_n$, where $m_1, \ldots, m_n$ ("planets") have comparable sizes, but much smaller than m_0 ("star", or "sun").

[5] The statement in [1] has been completely proved in [9]. The study has been reconsidered in [7] for open problems after [1,9].

$\mathcal{S}_0(\mathrm{r})$. Both such papers are rigorous proofs and are based well adapted normal form theory, so they unavoidably deal with ideal situations, where "ideal" means that the estimates on parameters are far from being optimal. In [3] the case (c) has been reconsidered from the numerical point of view and the existence of chaotic motions among librations has been pointed out.

This paper is organised as follows.

- In Section 2 we collect useful properties for the Hamiltonian (10).
- In Section 3 we discuss conditions (7) and (14) on two concrete examples.
- In Sections 4 and 5 we focus on one of the examples and study the phase space around two orbits. In particular, we study the variations of the function (16) around one orbit which spends much time closely to the saddle point (20) of one of the manifolds (19).
- In Section 6 we show the existence of chaos (in fact, of symbolic dynamics) in the region of the mentioned saddle point. This is the main result of the paper.
- In Section 7 we discuss how we control numerical errors, draw some conclusions and foresee possible future works.

2. Facts to be known

Let us consider the Hamiltonian $\mathrm{H}_{3\mathrm{b}}$ in (1), with $x_3 = x_3' = y_3 = y_3' = 0$. We define a canonical change of coordinates which reduces the invariance of $\mathrm{H}_{3\mathrm{b}}$ by rotations, via a canonical transformation

$$(\mathbf{y}', \mathbf{y}, \mathbf{x}', \mathbf{x}) \in \mathbb{R}^2 \times \mathbb{R}^2 \times \mathbb{R}^2 \times \mathbb{R}^2 \setminus \Delta \to (\mathrm{C}, \mathrm{G}, \Lambda, \mathrm{R}, \mathrm{c}, \mathrm{g}, \ell, \mathrm{r}) \in \mathbb{R}^3_+ \times \mathbb{R} \times \mathbb{T}^3 \times \mathbb{R}_+ \tag{22}$$

where

$$\Delta = \Big\{\mathbf{x} = \mathbf{0}\Big\} \bigcup \Big\{\mathbf{x}' = \mathbf{0}\Big\} \bigcup \Big\{\mathbf{x} - \mathbf{x}' = \mathbf{0}\Big\}$$

is the "collision set". To define the new coordinates at right hand side of (22), we denote as

- $\mathbf{i} = \begin{pmatrix} 1 \\ 0 \\ 0 \end{pmatrix}$, $\mathbf{j} = \begin{pmatrix} 0 \\ 1 \\ 0 \end{pmatrix}$ the directions of a orthonormal frame in $\mathbb{R}^2 \times \{\mathbf{0}\}$ and $\mathbf{k} = \mathbf{i} \times \mathbf{j}$ ("$\times$" denoting, as usual, the "skew-product"). We assume (11).
- after fixing a set of values of $(\mathbf{y}, \mathbf{x})$ where the Kepler Hamiltonian (4) takes negative values, let $\mathbb{E}$ denote the elliptic orbit with initial values $(\mathbf{y}_0, \mathbf{x}_0)$ in such set;
- $\mathbf{P}$, with $\|\mathbf{P}\| = 1$, the direction of the perihelion of $\mathbb{E}$, assuming $\mathbb{E}$ is not a circle;
- $\alpha_{\mathbf{w}}(\mathbf{u}, \mathbf{v})$ the oriented angle from $\mathbf{u}$ to $\mathbf{v}$ relatively to the positive orientation established by $\mathbf{w}$, if $\mathbf{u}$, $\mathbf{v}$ and $\mathbf{w} \in \mathbb{R}^3 \setminus \{\mathbf{0}\}$, with $\mathbf{u}, \mathbf{v} \perp \mathbf{w}$.

Then the coordinates at the right hand side of (22) are defined via

$$\begin{cases} \mathrm{C} = \|\mathbf{x} \times \mathbf{y} + \mathbf{x}' \times \mathbf{y}'\| \\ \mathrm{G} = \|\mathbf{x} \times \mathbf{y}\| \\ \mathrm{R} = \dfrac{\mathbf{y}' \cdot \mathbf{x}'}{\|\mathbf{x}'\|} \\ \Lambda = \sqrt{a} \end{cases} \qquad \begin{cases} \mathrm{c} = \alpha_{\mathbf{k}}(\mathbf{i}, \mathbf{x}') \\ \mathrm{g} = \alpha_{\mathbf{k}}(\mathbf{x}', \mathbf{P}) \\ \mathrm{r} = \|\mathbf{x}'\| \\ \ell = \text{mean anomaly of } \mathbf{x} \text{ in } \mathbb{E} \end{cases} \tag{23}$$

We recall that the mean anomaly of $\mathbf{x}$ is defined as the area of the elliptic sector spanned by $\mathbf{x}$ relatively to the perihelion of $\mathbb{E}$, normalised to 2π (refer to Fig. 1).

With a language which goes back to Liouville–Arnold theorem, the coordinates C, G and Λ will be called "actions", for being conjugated to c, g and ℓ, which take values in $\mathbb{T}$, hence, are called "angles". The coordinates (23) are singular when $\mathrm{G} = \Lambda$ (corresponding to vanishing eccentricity of $\mathbb{E}$. In that case, $\mathbf{P}$ is not defined) or $\mathrm{r} = 0$ (as c is not defined), so we should safely exclude such values from our domain. Observe however that the Hamiltonian (1) is c-independent by its discussed SO(2) invariance, and the singularity at $\mathrm{G} = \Lambda$ could be – if needed – easily eliminated switching to the "Poincaré" transformation $(\Lambda, \mathrm{G}, \ell, \mathrm{g}) \to (\Lambda, p, \lambda, q) = (\Lambda, \sqrt{2(\Lambda - \mathrm{G})}\cos \mathrm{g}, \ell + \mathrm{g}, -\sqrt{2(\Lambda - \mathrm{G})}\sin \mathrm{g})$. The canonical character of the coordinates (23) has been discussed, in a more general setting, in [2]. Using the coordinates (23), the Hamiltonian $\mathrm{H}_{3\mathrm{b}}$ turns to be c-independent, as the action C is a first integral for it. Then, we regard it as a "fixed parameter", skipping it from actions. Another first integral, namely the action Λ, appears when taking the ℓ-average of (1), as discussed in the previous section. In order to further simplify the discussion, it turns to be useful to remark the following scaling property. Switching to the a-dimensional and canonical coordinates

$$\widehat{\mathrm{R}} := \mathrm{R}\Lambda\,, \quad \widehat{\mathrm{G}} := \frac{\mathrm{G}}{\Lambda}\,, \quad \widehat{\mathrm{r}} := \frac{\mathrm{r}}{\Lambda^2}\,, \quad \widehat{\mathrm{g}} := \mathrm{g}$$

(possible because Λ is a "parameter") one has the following identities

$$\begin{aligned} &H_{C,\Lambda}(R, G, r, g) = \Lambda^{-2} H_{\widehat{C},1}(\widehat{R}, \widehat{G}, \widehat{r}, \widehat{g}) \\ &U_\Lambda(r, G, g) = \Lambda^{-2} U_1(\widehat{r}, \widehat{G}, \widehat{g}) \\ &E_\Lambda(r, G, g) = \Lambda^{2} E_1(\widehat{r}, \widehat{G}, \widehat{g}) \end{aligned} \tag{24}$$

with $\widehat{C}$ being the ratio $\frac{C}{\Lambda}$. The equalities in (24) allow us to assume (9) once forever and eliminate the "hats" and subfixes $_1$. As a result, $\overline{H}_C$ depends on 3 parameters only, namely α, β and C, and is reduced to 2 degrees of freedom, ruled by the coordinates (R, G, r, g). We provide the explicit expression of U, under the choice (9). Using, alternatively, the true anomaly ν and the eccentric anomaly ξ, we have

$$\begin{aligned} U(r, G, g) &= \frac{G^3}{2\pi} \int_0^{2\pi} \frac{d\nu}{(1 + e\cos\nu)\sqrt{r^2(1 + e\cos\nu)^2 - 2G^2 r(1 + e\cos\nu)\cos(g + \nu) + G^4}} \\ &= \frac{1}{2\pi} \int_0^{2\pi} \frac{(1 - e\cos\xi)d\xi}{\sqrt{(1 - e\cos\xi)^2 - 2r(\cos\xi - e)\cos g + 2rG\sin\xi\sin g + r^2}} \end{aligned} \tag{25}$$

with

$$e = \sqrt{1 - G^2}$$

being the eccentricity.

As a consequence of relation (15) and as E depends on g only via its cosinus while the other terms in (10) do not depend on g, we remark the following symmetry:

Proposition 2.1. *The Hamiltonian (10) does not change replacing* g *with* $2k\pi - g$, $k \in \mathbb{Z}$.

In fact, this symmetry reflects in all orbits of $\overline{H}_C$; see, e.g., the orbits Γ_s, Γ_u mentioned in Section 4.

As, in our experiments, we are going to consider a global region of phase space, we need to establish the singularities of U. Below, we shall briefly show that

Proposition 2.2 ([4,5,12])**.** *The function* U *is singular if and only if* $0 < r < 2$ *and* $(G, g) \in \mathcal{S}_0(r)$.

Namely, the manifold $\mathcal{S}_0(r)$ looses its meaning of saddle separatrix in the Hamiltonian (10) (discussed in the previous section) to gain the title of "singular manifold". In [12] the rate of divergence of U has been established to be logarithmic, with respect to the distance from $\mathcal{S}_0(r)$.

In this paper, we focus on a region of phase space where $0 < r < 1$, so as to deal with the respective cases (a) in Figs. 2–3. Ideally, we would be tempted to perform computations by replacing U with a polynomial

$$U_N(r, G, g) = \sum_{n=0}^{N} P_n(G, g) \cdot r^n \tag{26}$$

with sufficiently high degree N, provided to keep at a finite distance from $\mathcal{S}_0(r)$. However, in this expansion the coefficients $P_n(G, g)$ are proportional to negative powers of G, as one immediately recognises from (25). This means that regions in phase space with very small values of G would not be covered by such an approximation, while we precisely aim to look at such regions. On the other hand, by Proposition 2.2, $G = 0$ is not a singularity, if $g \neq \pi$ (as $(0, \pi)$ is the only point of $\mathcal{S}_0(r)$ with $G = 0$). Therefore, instead of (26), we consider a "renormalised" expansion of the form

$$U_N(r, G, g) = \sum_{n=0}^{N} Q_n(r, G, g) \cdot r^n \tag{27}$$

which differs from (26) by orders of r^{-N-1}. The expansion (27) is possible because of the relation (15). Indeed, by such relation, U depends on (G, g) only via E(r, G, g). Therefore, picking up, for any fixed level set (17) with $\mathcal{E} \geq 0$, the point of E with coordinates $(G, g) = (\sqrt{\mathcal{E}}, \frac{\pi}{2})$, we have the identity

$$F(r, \mathcal{E}) = U\left(r, \sqrt{\mathcal{E}}, \frac{\pi}{2}\right)$$

This identity reflects in the expansion (26), providing the expansion (27), with

$$Q_n(r, G, g) = P_n\left(\sqrt{E(r, G, g)}, \frac{\pi}{2}\right), \qquad \forall\ (r, G, g):\ E(r, G, g) \geq 0$$

From the procedural point of view, we remark that in the expansion (27) only the terms with $n = 2k$ even survive, as (as one readily sees using, e.g., a Legendre polynomials expansion) the function in (25) is even in r when $g = \frac{\pi}{2}$.

We conclude this section with the

Proof of Proposition 2.2. The first expression in (25) shows, for the function under the integral, a pole of order 1 (corresponding to the zero of the expression under the square root, and understood a collision between $\mathbf{x}$ and $\mathbf{x}'$) when the following equalities are satisfied

$$\nu = -\mathrm{g} \mod 2\pi\,, \qquad \mathrm{r}(1+e\cos\mathrm{g}) = \mathrm{G}^2 \tag{28}$$

and a pole of order 2 at $\nu = \pi$ when $\mathrm{G} = 0$ (corresponding to the zero of $(1+e\cos\nu)$ and understood a collision between $\mathbf{x}$ and the unit mass). Observe that the second equation in (28) is nothing else than the equation of $\mathcal{S}_0(\mathrm{r})$. The singularity at $\mathrm{G} = 0$ leaves instead U perfectly regular, as the second expression in (25) gives

$$\mathrm{U}(\mathrm{r},0,\mathrm{g}) = \frac{1}{2\pi}\int_0^{2\pi} \frac{(1-\cos\xi)d\xi}{\sqrt{(1-\cos\xi)^2 + 2\mathrm{r}(1-\cos\xi)\cos\mathrm{g} + \mathrm{r}^2}}$$

This shows that the only possibility of singularity for $\mathrm{U}(\mathrm{r},0,\mathrm{g})$ is when $0 < \mathrm{r} < 2$ and $\mathrm{g} = \pi$. But this is already counted in $\mathcal{S}_0(\mathrm{r})$. □

3. Discussion of (7) and (14) on two examples

In the introduction, we mentioned that the simultaneous fulfilment of inequalities (7) and (14) does depend *only* by choice of the parameters of the system — in our case, α, β and C, but also needs a careful choice of the phase space. In agreement with the numeric nature of the paper, in this section we investigate the question on two concrete examples. We pick two triples of values for α, β and C, and, for each triple, we consider motions of different kind. We check that, while the inequality (14) is met along all the orbits under examination, unfortunately, (7) is not.

Example 1

In the first example, we take[6]

$$\alpha = 100\,, \quad \beta = 120\,, \quad \mathrm{C} = 10\,. \tag{29}$$

In order to check (14) we consider two orbits, Γ_1 and Γ_2, of the Hamiltonian $\overline{\mathrm{H}}_\mathrm{C}$ in (10) on two *different* energy levels, $\mathcal{H}_1$, $\mathcal{H}_2$, of $\overline{\mathrm{H}}_\mathrm{C}$, but with initial data $(\mathrm{R}_i, \mathrm{G}_i, \mathrm{r}_i, \mathrm{g}_i)$ chosen so that the triplets $(\mathrm{r}_i, \mathrm{G}_i, \mathrm{g}_i)$ coincide with the saddle points (20) of the manifolds $\mathcal{M}(\mathcal{E}_i)$, with

$$\mathcal{E}_i = \mathrm{E}(\mathrm{r}_i, \mathrm{G}_i, \mathrm{g}_i) = \begin{cases} 0.2 & \text{if} \quad i = 1 \\ \\ 0.8\bar{3} & \text{if} \quad i = 2 \end{cases}\,.$$

In fact, we take

$$\mathcal{H}_1 := 613.75\,, \qquad \Gamma_1 : \begin{cases} \mathrm{R}_1 = 0 \\ \mathrm{G}_1 = 0 \\ \mathrm{r}_1 = 0.2 \\ \mathrm{g}_1 = \pi \end{cases}\,, \tag{30}$$

$$\mathcal{H}_2 := -155.025\,, \qquad \Gamma_2 : \begin{cases} \mathrm{R}_2 = 0 \\ \mathrm{G}_2 = 0 \\ \mathrm{r}_2 = 0.8\bar{3} \\ \mathrm{g}_2 = \pi \end{cases}\,. \tag{31}$$

We remark that $\mathcal{E}_1$ has been chosen so that K_C is initially positive, while $\mathcal{E}_2$ has been chosen so that K_C is initially negative (in fact, at its[7] minimum).

In order to check (7), we consider the orbits $\widetilde{\Gamma}_1$ and $\widetilde{\Gamma}_2$, of the whole Hamiltonian $\mathrm{H}_{3\mathrm{b,C}}$ in (6), departing from the initial data obtained completing the respective initial values of Γ_1 and Γ_2 with $\Lambda_i = 1$ (as prescribed in (9)) and $\ell_i = \pi$.

The results are plotted in Figs. 5 and 6. Fig. 5 shows that, along Γ_2, K_C remains "encapsulated" at its initial value for much longer a time than along Γ_1, a somewhat expected fact. However, for the part of the graph represented in such figures, relations (14) are well maintained along Γ_1 and Γ_2 as well. Fig. 6 clearly says that, unfortunately, the inequality in (7) does not hold nor along $\widetilde{\Gamma}_1$ or along $\widetilde{\Gamma}_2$.

[6] We recall that α, β are the two independent mass parameters and they are uniquely linked to κ, μ which turn out to be $\kappa = 0.01787503$, $\mu = 0.02153618$.

[7] As well known, K_C attains its minimum, given by $-\frac{\beta^2}{2\mathrm{C}^2}$, when $\mathrm{R} = 0$ and

$$\mathrm{r} = \frac{\mathrm{C}^2}{\beta} = \frac{100}{120} = 0.8\bar{3}.$$

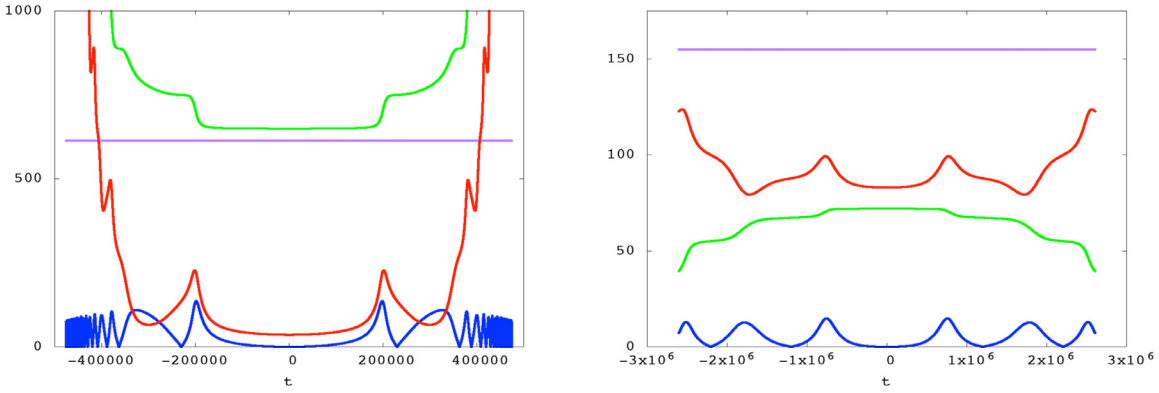

Fig. 5. Graphs of the absolute values of K_C (green), αU (red) and $\widetilde{K}_C$ (blue) along Γ_1 (left) and Γ_2 (right). The purple line, representing the total energy (10), is reported for comparison. Incidentally, plotting the total energy is a well known useful tool to check the correctness of numerical integrations.

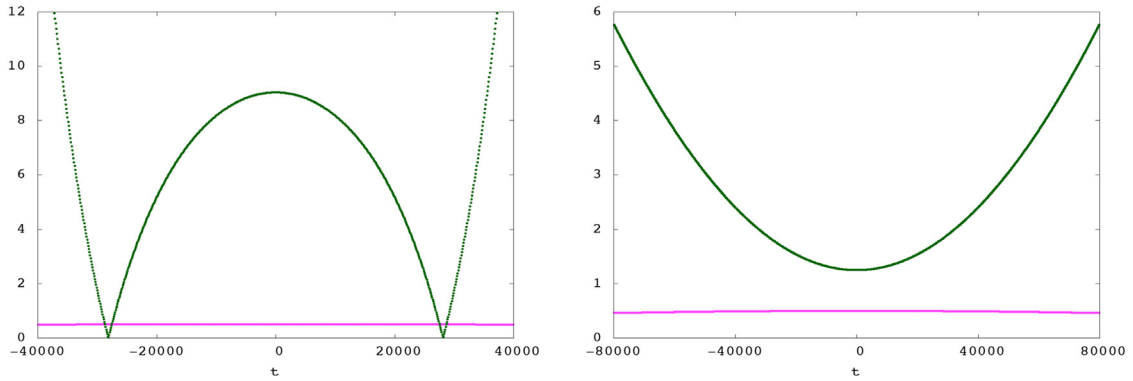

Fig. 6. Graphs of the absolute values of $\widetilde{H}_C$ (green) and $\left\| -\frac{1}{2\Lambda^2} \right\|$ (pink) along $\widetilde{\Gamma}_1$ (left) and $\widetilde{\Gamma}_2$ (right).

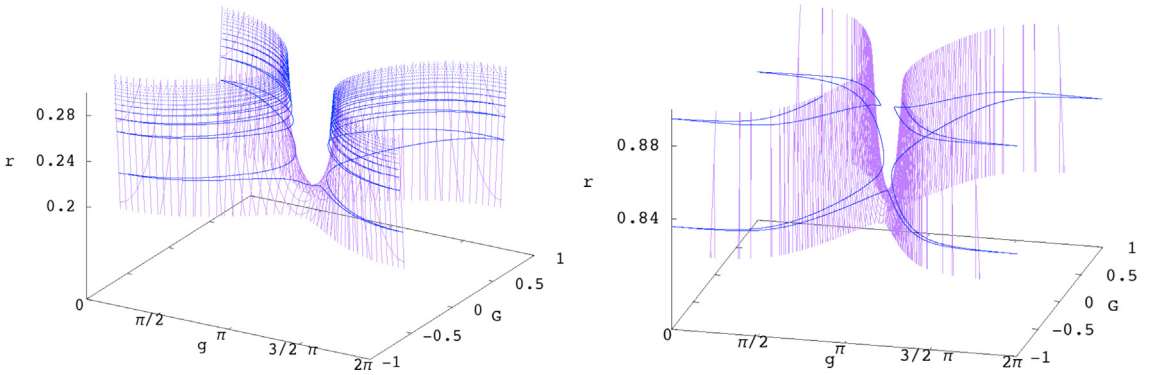

Fig. 7. Orbits Γ_1 (left) and Γ_2 (right) in blue and the respective manifolds $\mathcal{M}(\mathcal{E}_1)$, $\mathcal{M}(\mathcal{E}_2)$ in purple.

Example 2

We choose[8]

$$\alpha = 50\,, \quad \beta = 20\,, \quad C = 1.6 \tag{32}$$

[8] In this case κ, μ turn out to be $\kappa = 0.06814254$, $\mu = 0.02725702$.

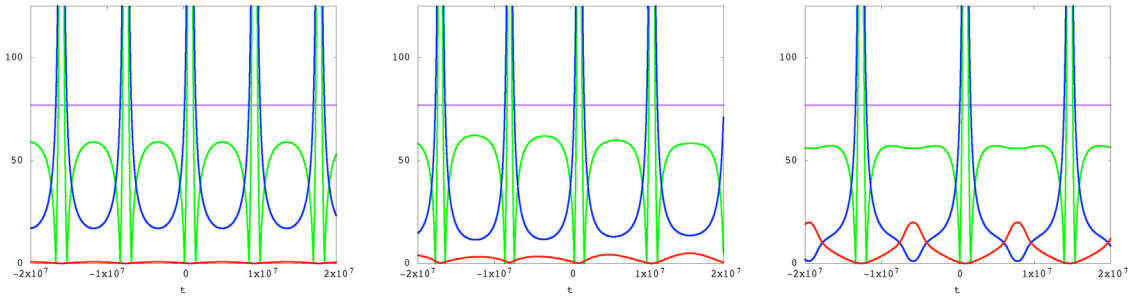

Fig. 8. Graphs of the absolute values of K_C (green), αU (red) and $\widetilde{K}_C$ (blue) along Γ_s (left), Γ_0 (centre), Γ_u (right). The purple line represents the total energy (10).

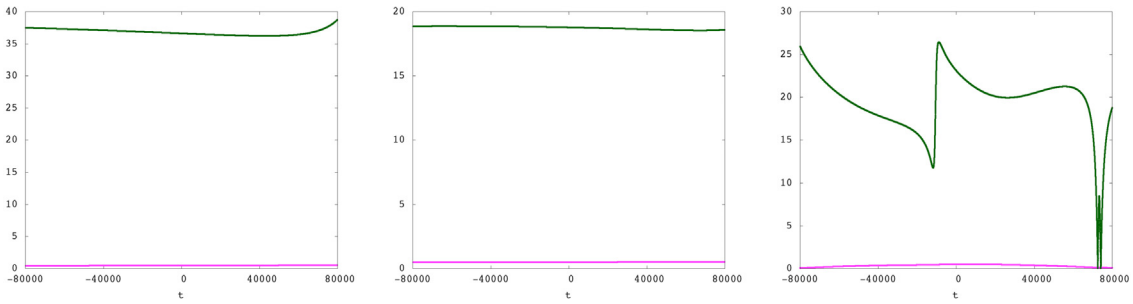

Fig. 9. Graphs of the absolute values of $\widetilde{H}_C$ (green) and $\left\| -\frac{1}{2\Lambda^2} \right\|$ (pink) along $\widetilde{\Gamma}_s$ (left), $\widetilde{\Gamma}_0$ (centre), $\widetilde{\Gamma}_u$ (right).

and we fix the energy level for the Hamiltonian (10) with the value

$$\mathcal{H} = -76.887\,. \tag{33}$$

On such energy level, we choose three orbits, which we denote as Γ_s, Γ_0 and Γ_u, respectively determined by the following initial data

$$\Gamma_s : \quad \begin{cases} R_s = -11.367 \\ G_s = 0.993 \\ r_s = 0.132 \\ g_s = 2.759 \end{cases}, \tag{34}$$

$$\Gamma_0 : \quad \begin{cases} R_0 = -9.075 \\ G_0 = 0.5 \\ r_0 = 0.132 \\ g_0 = \pi \end{cases}, \tag{35}$$

$$\Gamma_u : \quad \begin{cases} R_u = 10.331 \\ G_u = 0.718 \\ r_u = 0.132 \\ g_u = 5.699 \end{cases}. \tag{36}$$

As in the previous example, inequality (7) is illustrated on the orbits $\widetilde{\Gamma}_s$, $\widetilde{\Gamma}_0$ and $\widetilde{\Gamma}_u$ of the whole Hamiltonian $H_{3b,C}$ in (6), departing from initial data obtained completing the respective initial data of Γ_s, Γ_0 and Γ_u with $\Lambda_i = 1$ and $\ell_i = \pi$.

The results are plotted in Figs. 8 and 9. In Fig. 8, the zones where K_C and $\widetilde{K}_C$ diverge correspond to the coordinate r approaching 0. As a consequence, we have that (14) is not satisfied on the entire orbits, but only on the portion around the maximum of $|K_C|$, which corresponds with the zone around the minimum of $|\widetilde{K}_C|$. As in the previous example, Fig. 9 shows that the inequality in (7) is not met along any of the orbits $\widetilde{\Gamma}_s$, $\widetilde{\Gamma}_0$ and $\widetilde{\Gamma}_u$.

As mentioned above, notwithstanding the negative results of Figs. 6 and 9, justified by the considerations in the introduction, from now on, we focus on the dynamical properties of the Hamiltonian $\overline{H}_C$ in (10). Our goal is to check slow variations of the Euler integral in some chosen region of phase space and co-existence of chaotic phenomena. At this respect, we remark that, even though Fig. 5 of Example 1 is encouraging, proving existence of chaos closely to $\mathcal{M}_0$ along this way seems really hard. The difficulty is that, even though the initial point of Γ_i has been chosen *precisely* on the saddle of $\mathcal{M}(\mathcal{E}_i)$, and, for a long time, the orbits maintains to be very close to $\mathcal{M}(\mathcal{E}_i)$, however, the coordinate r increases such in a way to leave the region $0 < r < 1$ (hence, the region of the saddle) in a short time; see Fig. 7. For this reason,

Table 1
Values of fixed points.

(G_s, g_s)	$(0.992515, 0.878179\,\pi)$
(G_u, g_u)	$(0.717909, 1.81405\,\pi)$

Table 2
Eigenvalues of fixed points (G_s, g_s) and (G_u, g_u).

	Eigenvalue 1	Eigenvalue 2
(G_s, g_s)	$0.99568665 + i\,0.99278032$	$0.99568665 - i\,0.99278032$
(G_u, g_u)	-0.051632609	-19.366447

in the rest of the paper we shall be focused on the orbits Γ_s and Γ_u in Example 2, where the motion of r is sufficiently slow.

4. The orbits Γ_s and Γ_u

Let us consider the Hamiltonian (10), with α, β and C as in (32). We fix the value $\mathcal{H}$ of the energy as in (33) and we reduce the coordinate R via

$$R = \pm\sqrt{2\left(\mathcal{H} - \alpha U(r, G, g) - \frac{(C-G)^2}{2r^2} + \frac{\beta}{r}\right)}, \tag{37}$$

with the sign being chosen by continuity. We look at the motion of the triplet (r, G, g) in a 3-dimensional space.

We empirically find a periodic orbit of H in (10) in correspondence of the initial datum (34). We denote as Γ_s the projection of such orbit in the space (r, G, g). We choose Π_s as the plane orthogonal to Γ_s at (r_s, G_s, g_s). We construct a 2-dimensional map

$$\mathcal{P}_{\mathcal{H},\Pi_s}: \qquad (G, g) \to (G', g') \tag{38}$$

where (G', g') is the first return value on Π_s. By construction, (G_s, g_s) is a fixed point of $\mathcal{P}_{\mathcal{H},\Pi_s}$. The images of the map $\mathcal{P}_{\mathcal{H},\Pi_s}$ with Π_s as said are depicted in Fig. 10, left. A Newton Algorithm is used to find other fixed points, besides (G_s, g_s). Another point is actually found (G_u, g_u), which (using the equation of Π_s and of the energy reduction (37)) unfolds to the quadruplet (36). Amazingly, we did not find other fixed points of $\mathcal{P}_{\mathcal{H},\Pi_s}$:

Numerical Evidence 4.1. *If $\mathcal{H}$ is as in (33) and Π_s is orthogonal to Γ_s at (r_s, G_s, g_s), then (G_s, g_s), (G_u, g_u) are the only fixed points of $\mathcal{P}_{\mathcal{H},\Pi_s}$.* □

In Table 1 we report the value of the two fixed points. This is to be compared with the situation studied in [3], where several hyperbolic points in a chaotic region were numerically detected.

The computation of the eigenvalues of the linear part of $\mathcal{P}_{\mathcal{H},\Pi_s}$ at (G_s, g_s) and (G_u, g_u) assigns to (G_s, g_s) the character of elliptic fixed point (for having complex eigenvalues), and to (G_u, g_u) the character of hyperbolic fixed point (for having real eigenvalues, one inside, one outside the unit circle) for $\mathcal{P}_{\mathcal{H},\Pi_s}$ (see Table 2).

Therefore, we shall refer to the periodic orbits Γ_s, Γ_u through (r_s, G_s, g_s), (r_u, G_u, g_u) in the space (r, G, g) as "elliptic", "hyperbolic" periodic orbit, respectively. Such orbits are depicted in Fig. 10, right, where also the plane Π_s is visualised.

In the next, in order to study the validity of Conjecture 1.3, (i), we study how the Euler integral changes along such orbits. We shall see that Γ_s is immersed in a region of phase space close to $\mathcal{M}_1$ at all times, while Γ_u spends much time close to $\mathcal{M}_0$.

Spread of E about Γ_s

In the top panel of Fig. 11, the time variations of R, G, r, g along Γ_s are represented. In particular, g spans $[0, 2\pi]$ while G has a very short range of variation (the relative variation changes periodically by a factor of order of 10^{-4}, so it turns to be quasi-constant). In the bottom panel, we have represented the motion in the planes (R, r), (G, g), (r, g) and the variation of E along the orbit. The latter plot shows that E varies a little, taking values very close to 1. This means that the orbit is in a zone of phase space very close to $\mathcal{S}_1(r)$ (see (18)) with r taking the mentioned values.

In order to inspect the variations of E in a neighbourhood of Γ_s, we proceed as follows. We choose a grid of initial conditions (R_0, G_0, r_0, g_0) on the same energy level (33), and verifying

$$(r_0, G_0, g_0) \in \mathcal{M}_1 \tag{39}$$

(with $\mathcal{M}_1$ as in (21)) and let the system evolve under $\overline{H}_C$. Then in the plane (G, g) we mark a point whenever $(G, g) \in \mathcal{S}(r_0, \theta)$, with $\mathcal{S}(r, \mathcal{E})$ as in (17) for the initial values in the grid. We find that

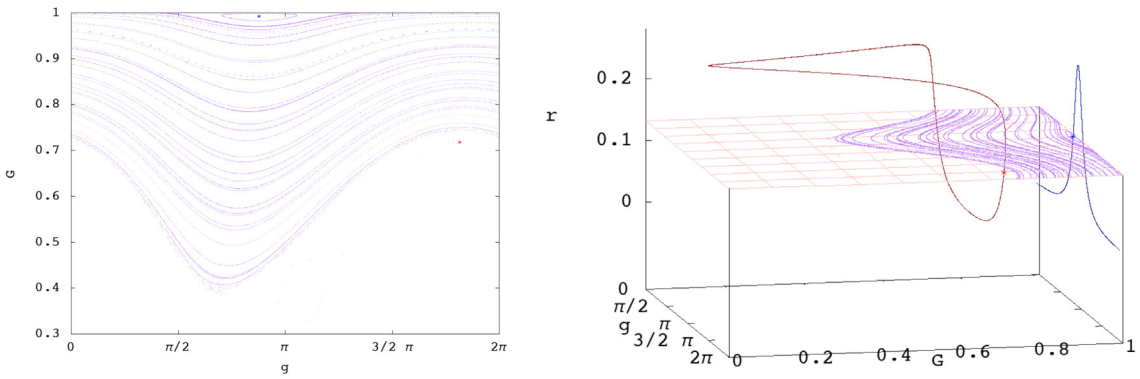

Fig. 10. Left: the Poincaré map (38) with $\mathcal{H}$ in (33) and Π_s orthogonal to Γ_s at (r_s, G_s, g_s). Right: spatial visualisation with Γ_s, Γ_u in blue and in red, respectively.

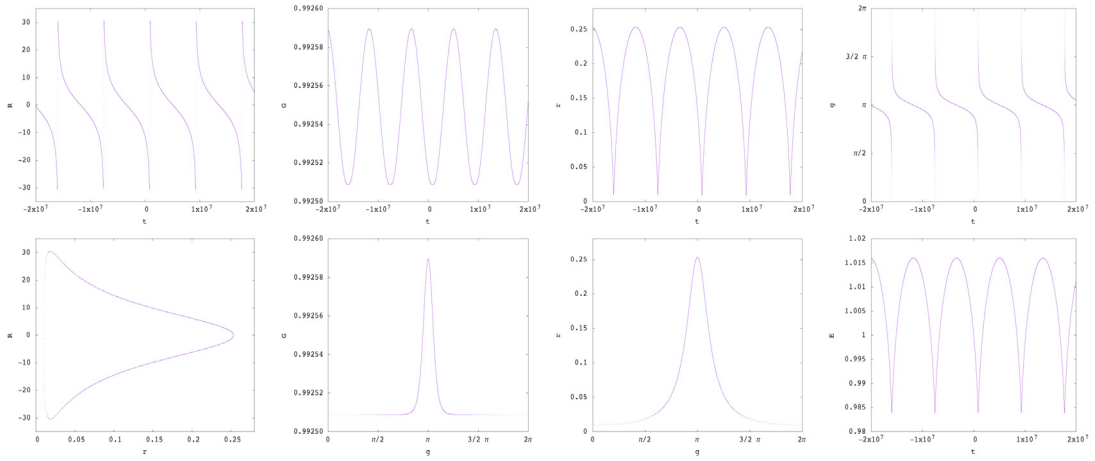

Fig. 11. Details on the orbit Γ_s.

Numerical Evidence 4.2. *The only non void level manifolds $\mathcal{M}(\theta)$ intersected by orbits of $\overline{\mathrm{H}}_C$ with initial data in $\mathcal{M}_1$ are those with*

$$\theta \in [0.91, 1.01]\,. \quad \square \tag{40}$$

We report the results in Fig. 12 (top), with the purple curve corresponding to $\theta = 1$ and the blue curves to different values of θ in (40). The red point in the figure represents (G_s, g_s).

We also provide a spatial visualisation, reporting in Fig. 12 (bottom) manifolds $\mathcal{M}(\theta)$ in (19) which are intersected by the time evolution of initial data in $\mathcal{M}_1$, with θ as in (40).

Spread of E about $\boldsymbol{\Gamma_u}$

The time variations of the coordinates R, G, r and g along the hyperbolic periodic orbit are depicted in the upper panel of Fig. 13. The bottom panel, from left to right, shows the hyperbolic orbit in the planes (R, r) and (G, g); the time variation of E along the orbit compared with the variation of variable r. Due to the variation of the velocity along the orbit, E spends most of time "close" to its initial value. With this we mean that, if T the period of the orbit, and $T_{20\%}$, $T_{5\%}$, $T_{1\%}$ the time when, respectively, the variation of E is less than 20% (straight line blue in right bottom plot in Fig. 13), less than 5% (straight line dark-green in the same plot) and less than 1% (straight line green), the follow relations hold:

$$T_{20\%} = 41.5\% \cdot T \quad , \quad T_{5\%} = 19.4\% \cdot T \quad , \quad T_{1\%} = 10.9\% \cdot T.$$

Moreover, in Fig. 13 bottom–third from left, we note that the Euler integral E of the hyperbolic orbit reaches its minimum E_{min} when r is maximum and its maximum E_{max} when r is minimum. Moreover, the maximum value r_{max} of r is slightly less than the minimum E_{min} of E, as in fact

$$r_{max} = \varrho_0 E_{min}, \qquad \varrho_0 = 0.991.$$

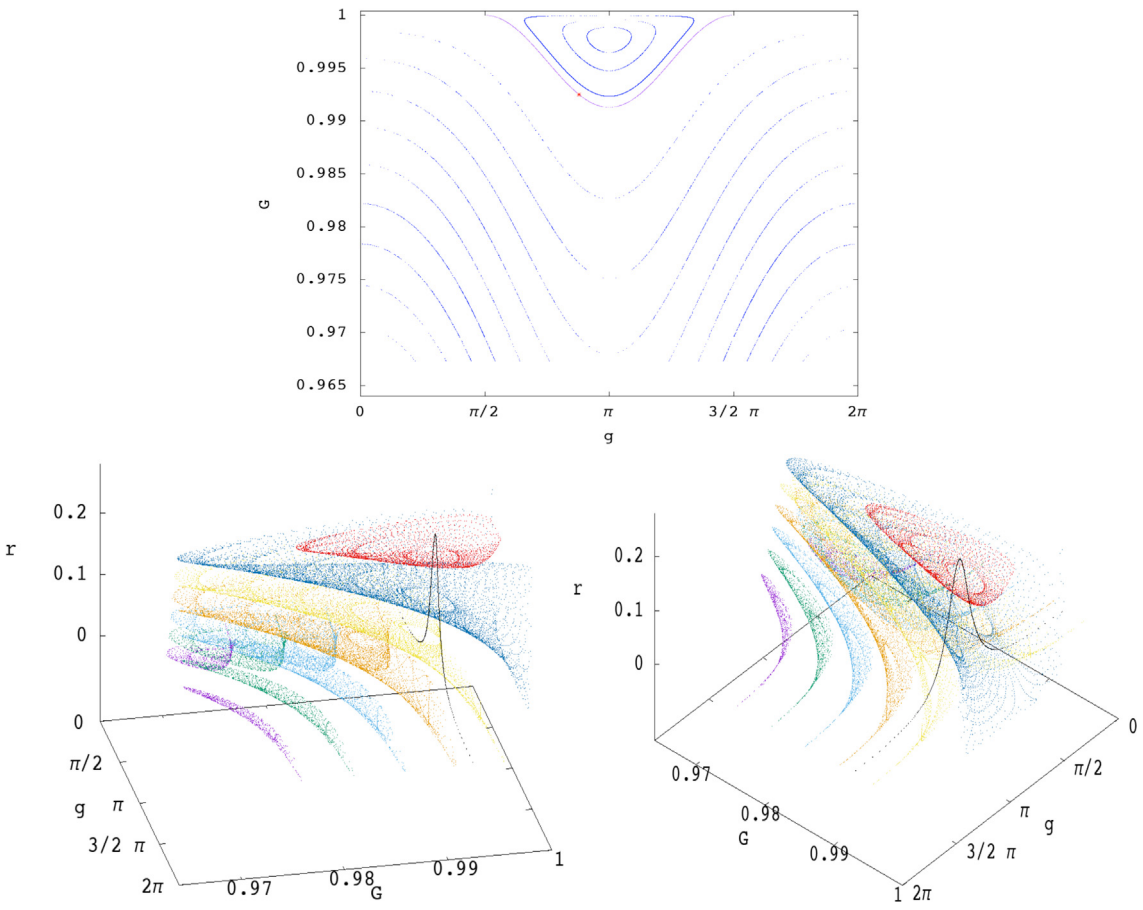

Fig. 12. Curves (top) $\mathcal{S}(r_0, \theta)$ and manifolds (bottom) $\mathcal{M}(\theta)$ intersected by the $\overline{H}_C$ evolution, with initial data $(r_0, G_0, g_0) \in \mathcal{M}_1$, and the curve Γ_s.

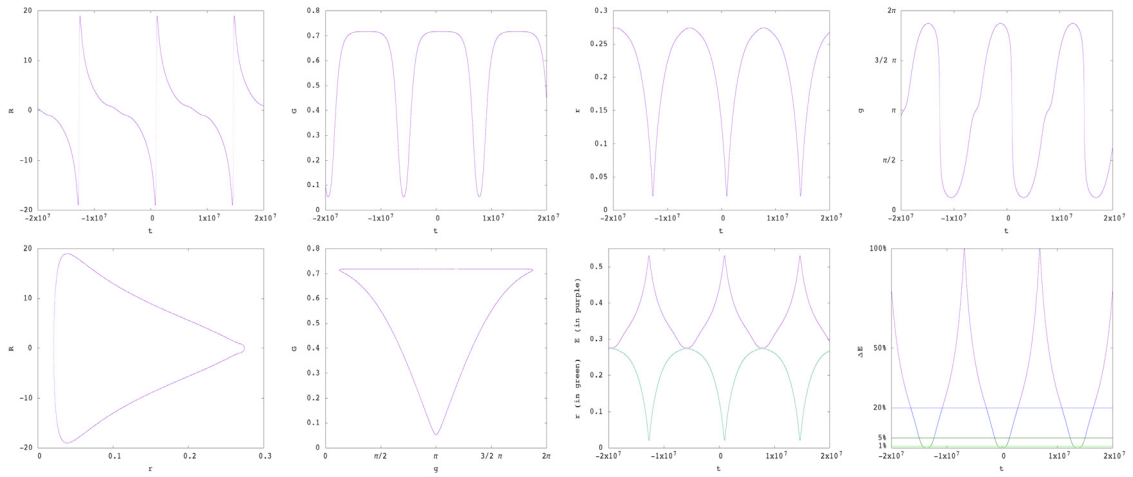

Fig. 13. Evolution of the periodic hyperbolic orbit. Upper from left to right, respectively, variables (R, G, r, g) versus time. Bottom from left to right: orbit in the planes (R, r), (G, g), respectively; variation of the Euler integral (in violet) compared with variable r (in green); percentage variations of Euler integral (in blue less than 20%, in dark-green less than 5%, in green less than 1%).

In particular, E reaches its minimum along the orbit in a region of phase space which is very close to $\mathcal{S}_0(r_{max})$. Analogously to the case of the elliptic orbit, we plot, in the plane (G, g), level curves $\mathcal{S}(r_{max}, \varrho \cdot E_{min})$ intersected by the $\overline{H}_C$-evolution under a grid of initial values $(r_0, G_0, g_0) \in \mathcal{M}(E_{min})$. We find that

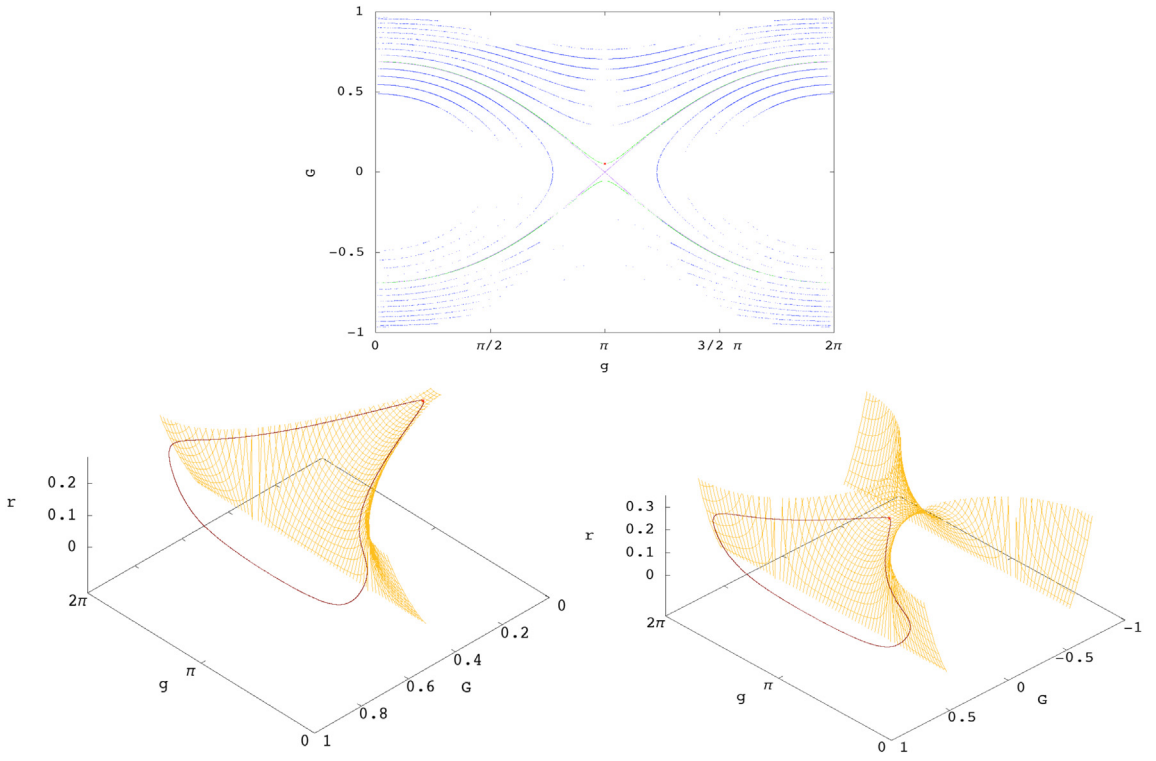

Fig. 14. Top: curves $\mathcal{S}(r_0, \varrho E_{min})$ intersected by the $\overline{H}_C$ evolution, with initial data $(r_0, G_0, g_0) \in \mathcal{M}(E_{min})$. Bottom: position of Γ_u relatively to the manifold $\mathcal{M}(E_{min})$.

Numerical Evidence 4.3. *The only non void level manifolds $\mathcal{M}(\varrho E_{min})$ intersected by orbits of $\overline{H}_C$ with initial data in $\mathcal{M}(E_{min})$ are those with*

$$\varrho \in [0\,,\ 3.1]\,. \quad \square \tag{41}$$

We report the results in Fig. 14, top. By construction, the value (marked in red) of (G, g) on Γ_u at the time when $E = E_{min}$ belongs to the curve (plotted in green) with $\varrho = 1$, while $\mathcal{S}_0(r_{max})$ is obtained for $\varrho = 0.991$ (plotted in purple). In blue, we plot curves for different values of ϱ in (41). For comparison, in Fig. 14, bottom, we report the position of Γ_u relatively to the manifolds $\mathcal{M}(E_{min})$ (yellow). We note that ϱE_{min} with $\varrho = 3.1$ corresponds at $\mathcal{E} = 0.858673$ which is less than the minimum admissible value provided in Numerical Evidence 4.2.

Finally, in order to measure how the level manifolds $\mathcal{M}(\mathcal{E})$ which are "touched" by Γ_u spread under $\overline{H}_C$, we proceed as follows. We pick a box of initial values (R_0, G_0, r_0, g_0) on the energy level (33) and $(r_0, G_0, g_0) \in \mathcal{M}(E_{min})$ and let the system evolve under $\overline{H}_C$. We mark a point on the three-dimensional space (r, G, g) whenever the orbits intersects $\mathcal{M}(\mathcal{E})$, with

$$\mathcal{E} \in \left\{E_{min},\ E_{mid}\,,\ E_{max}\right\} \tag{42}$$

where E_{min}, E_{mid}, E_{max} are, respectively, the minimum (0.276991), middle (0.438944), maximum (0.530668) value of E along Γ_u (see Fig. 13). We obtain the picture in Fig. 15, bottom, where the orange is for $\mathcal{M}(E_{min})$, magenta is for $\mathcal{M}(E_{mid})$ and red for $\mathcal{M}(E_{max})$.

In Fig. 16, Γ_u is plotted and we report in blue the part of the orbit such that E – along the orbit – varies less than 20% compared to its minimum value E_{min}, in dark-green the part with variation less than 5% and in green the part with variation less than 1% (compare with last plot in Fig. 13).

We conclude this section with a visualisation of the "spread of E" about Γ_s and Γ_u. In Fig. 17 we plot manifolds $\mathcal{M}(\mathcal{E})$ intersected under the $\overline{H}_C$-evolution, with initial data in $\mathcal{M}(\mathcal{E})$, with $\mathcal{E}$ as in Fig. 12 (light blue) and (42) (orange to red).

5. Neighbourhoods of Γ_u

In this section, we show several 2-dimensional maps associated with Γ_u, but constructed in different ways, and detect chaotic phenomena.

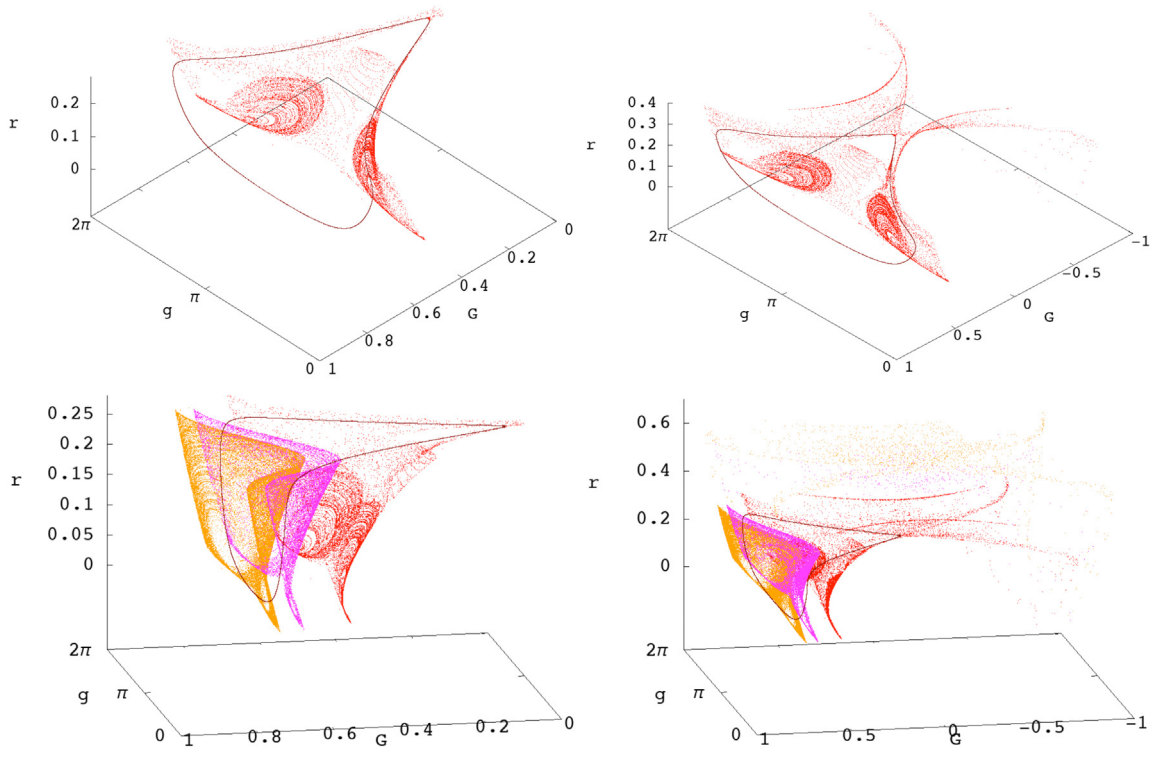

Fig. 15. Top: details on the positions of Γ_u and the part of $\mathcal{M}(E_{min})$ intersected by orbits evolving from $\mathcal{M}(E_{min})$ under $\overline{H}_C$. Bottom: manifolds $\mathcal{M}(\mathcal{E})$ intersected by the $\overline{H}_C$ evolution, with initial data $(r_0, G_0, g_0) \in \mathcal{M}(E_{min})$, with $\mathcal{E} \in \{E_{min},\ E_{mid},\ E_{max}\}$.

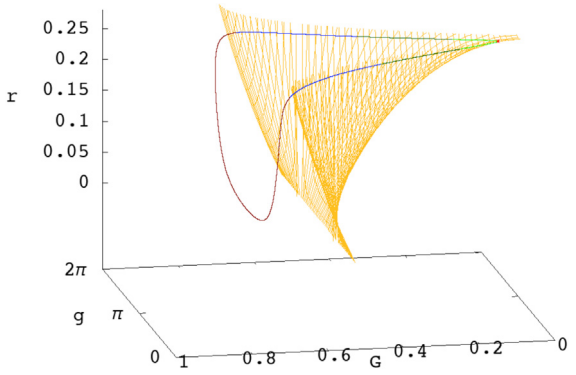

Fig. 16. Variations of Euler integral (in blue less than 20%, in dark-green less than 5%, in green less than 1%) along the orbits Γ_u related to $\mathcal{M}(E_{min})$.

1. The first map is $\mathcal{P}_{\mathcal{H},\Pi_s}$, in (38), defined, we recall, as the first return map on a plane Π_s orthogonal to the orbit Γ_s in Fig. 12 at the point (r_s, G_s, g_s), defined as in (34). As outlined in the Numerical Evidence 4.1, the map $\mathcal{P}_{\mathcal{H},\Pi_s}$ does not show other fixed point than (G_s, g_s) and (G_u, g_u). We find the following

Numerical Evidence 5.1 (*Transverse Homoclinic Intersection for* $\mathcal{P}_{\mathcal{H},\Pi_s}$)**.** *The stable*[9] *and unstable manifolds departing from and arriving at* (G_u, g_u) *under* $\mathcal{P}_{\mathcal{H},\Pi_s}$ *have transverse intersection.* □

[9] We recall that local stable and unstable manifolds associated to the hyperbolic fixed point $\mathbf{x}^*$ of a map $\mathcal{P}$ are defined as

$$\mathcal{W}^s_{loc} = \left\{ x \;\middle|\; \|\mathcal{P}^n(x) - x^*\| \to 0,\ \ n \in \mathbb{N}_+ ,\ n \to \infty \right\},$$
$$\mathcal{W}^u_{loc} = \left\{ x \;\middle|\; \|\mathcal{P}^{-n}(x) - x^*\| \to 0,\ \ n \in \mathbb{N}_+ ,\ n \to \infty \right\}.$$

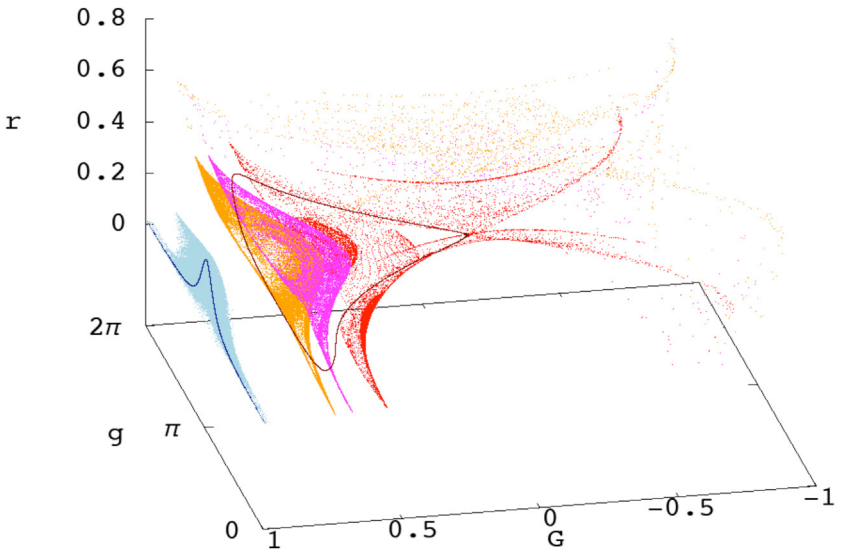

Fig. 17. Comparison between the spread of E associated to Γ_s (light blue) and Γ_u (orange to red).

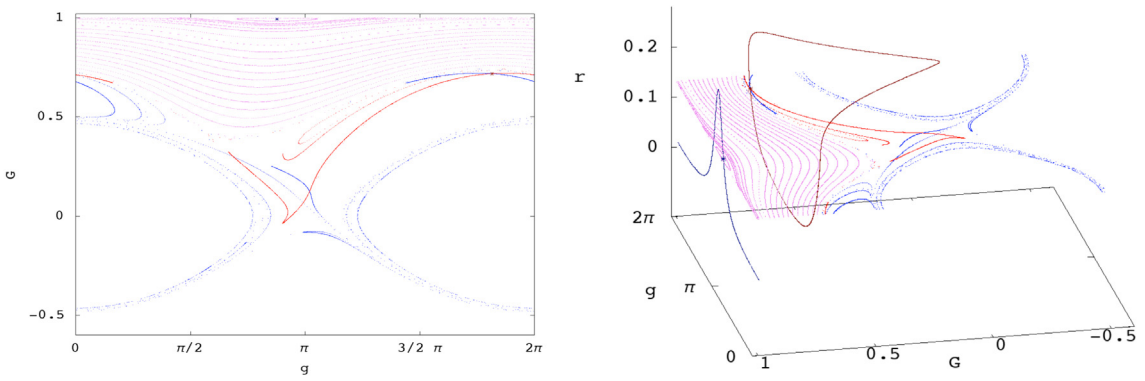

Fig. 18. Plane (left) and spatial (right) visualisation of $\mathcal{P}_{\mathcal{H},\Pi_s}$.

At this respect, in Fig. 18 the following objects are visible:

- the elliptic (dark-blue) and the hyperbolic (dark-red) fixed points;
- rotational tori (purple);
- chaotic motions (dotted purple);
- the transverse homoclinic intersection between the stable (blue) and unstable (red) manifolds from (G_u, g_u).

2. Let Π_u^i be different planes orthogonal to Γ_u at different points (r_i, G_i, g_i) of the curve. We consider first return maps

$$\mathcal{P}_{\mathcal{H},\Pi_u^i}: \qquad (G, g) \to (G', g') \tag{43}$$

along Π_u^i. Incidentally, this procedure provides us with an help to control numerical errors, as we check the invariance of the Lyapunov exponents at (G_*^i, g_*^i), for different choices of Π_u^i.

We denote as Π_* the plane orthogonal to Γ_u at

$$(r_*, G_*, g_*) = (0.270, 0.346, 1.27\,\pi) \tag{44}$$

This point of Γ_u has been chosen for being "close" to $\mathcal{M}_0$. With this choice, we detect a homoclinic tangency and absence of splitting:

Numerical Evidence 5.2 (*Quasi-Homoclinic Tangency*)**.** *Consider first return maps* (43) *on* Π_u^i*. As soon as* r_*^i *is chosen closer and closer to* r_{max} *the stable tori zone becomes smaller and smaller. For* $\Pi_u^i = \Pi_*$*, stable motions are not numerically detected,*

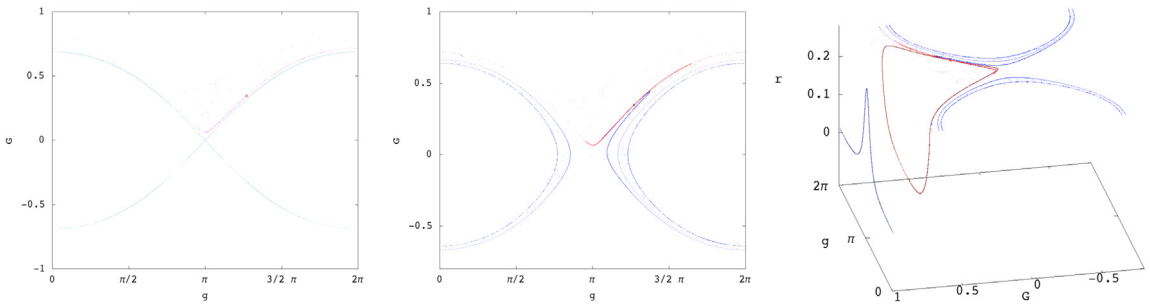

Fig. 19. First return map on the plane Π_* orthogonal to Γ_u at (r_*, G_*, g_*).

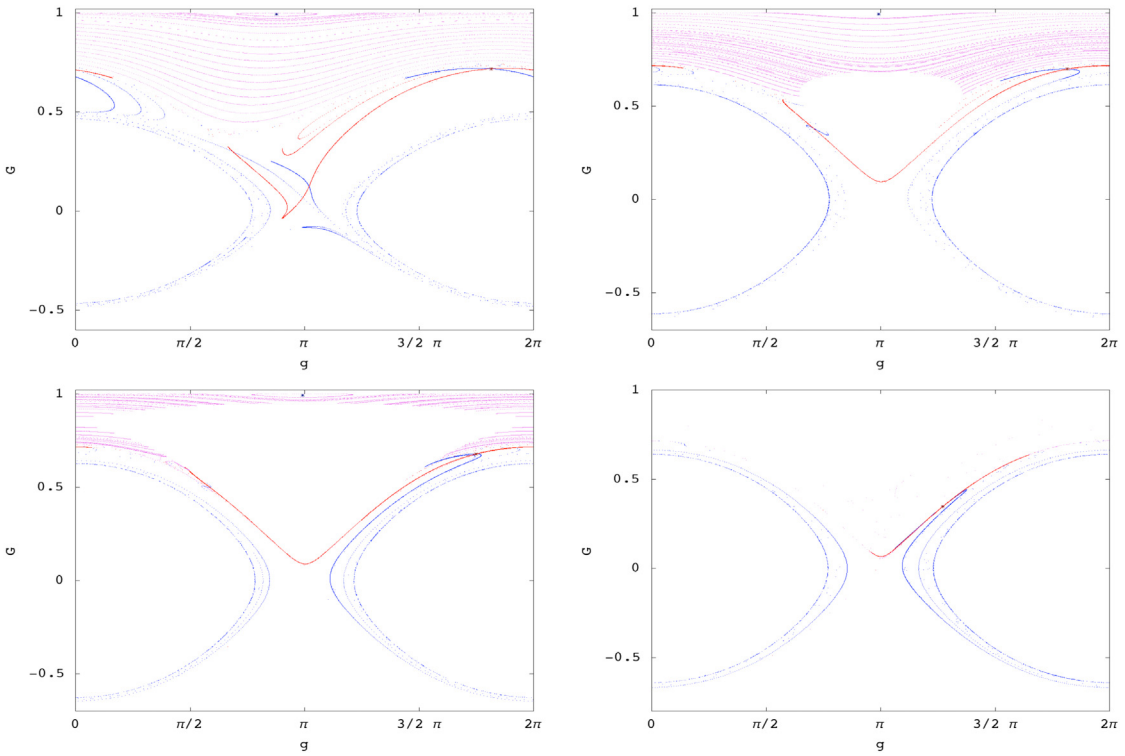

Fig. 20. First return maps on the planes Π_u^i orthogonal to Γ_u at $(r_i, G_i, g_i) \in \Gamma_u$, for $i = 1, \dots, 4$ where, from upper left to bottom right, respectively, $r_1 = 0.13165$, $r_2 = 0.242432$, $r_3 = 0.252024$, $r_4 = r_* = 0.26987$ (we recall that $r_{max} = 0.274496$).

and the unstable, stable manifolds have a homoclinic tangency at (G_*, g_*)*. In other words a splitting of such manifolds (which have the shape of* $\mathcal{S}_0(r_*)$*) is not numerically detected.* □

The normalised stable and unstable eigenvectors in (G_*, g_*) are, respectively,

$$v_*^s = (0.312937\,,\ 0.949774)\,, \quad v_*^u = (0.320019\,,\ 0.947411,\,)$$

and the angle between them is

$$\alpha = 0.0074651.$$

The results are visualised in Fig. 19 and 20.

3. We finally fix the plane $\Pi^* = \{g = g_*\}$. The two-dimensional first return map

$$\mathcal{P}_{\mathcal{H},\Pi^*}: \qquad (r, G) \to (r', G') \tag{45}$$

is depicted in Fig. 21. The aspect of the stable and unstable manifolds changes drastically, but homoclinic intersections are present.

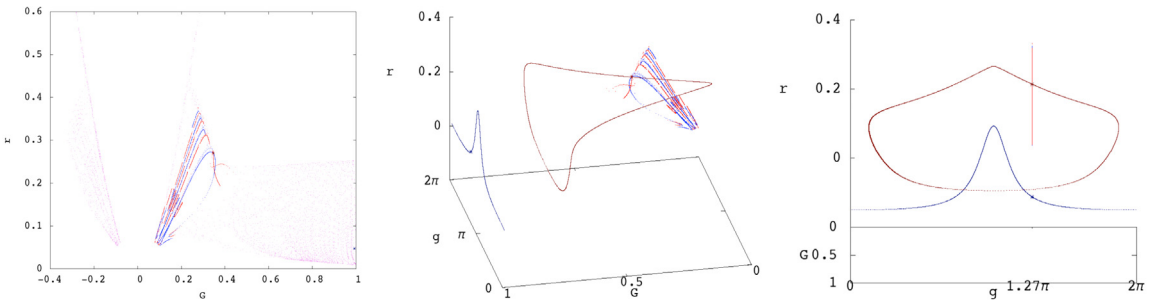

Fig. 21. First return map on the plane $\Pi^* = \{g = g_*\}$. Note the aspect of the stable and unstable manifolds in the first panel.

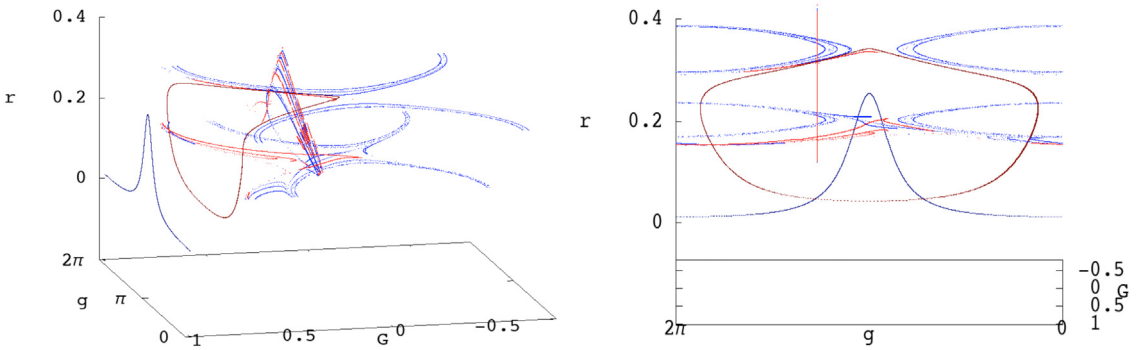

Fig. 22. Stable (in blue) and unstable (in red) manifolds constructed using different maps.

A comprehensive visualisation including the surface sections and returns maps herewith considered is in Fig. 22.

4. As special case of previous point, we fix the plane $\Pi^\star = \{g = \pi\}$. Due to the geometrical shape and properties of the curve Γ_u, it is not possible to fix the orthogonal planes at the points $T = (G_\star, r_{min}, \pi)$ and $S = (G^\star, r_{max}, \pi)$. For this reason, we study the structure of the first return map on the plane $\Pi^\star$. The points T, S are both hyperbolic fixed points depending on the orbit is run in one direction or in the opposite. We construct stable and stable manifolds for both fixed points and we obtain a complete overlapping of the stable and unstable manifolds of each point. In Fig. 23, we can see in red and blue the manifolds related to S (and the blue manifold is completely hidden by the red one) and in orange and light-blue the manifolds related to T.

6. Symbolic dynamics

In this section, we discuss numerical evidence of symbolic dynamics for the map $\mathcal{P}_{\mathcal{H},\Pi^*}$ in (45), in the sense of the following

Definition 6.1 (*Symbolic Dynamics; Horseshoe*)**.**Let $D \subset \mathbb{R}^2$

$$f : \quad D \to \mathbb{R}^2 ,$$

we say that f has *m-symbolic dynamics* if there exist compact subsets with non-empty interior $N_0, N_1 \subset D$ such that, for every $n \in \mathbb{N}$ and any finite sequence $(\sigma_0, \ldots, \sigma_n)$ of symbols $\sigma_i \in \{0\,,\ 1\}$ having length $n+1$, one can find $x_0 \in N_{\sigma_0}$ such that the orbit of x_0 under f, namely, $x_j := f^j(x_0)$ is well defined for $j = 0, \ldots,$ nm, and $x_{mj} \in N_{\sigma_j} \quad \forall\, j = 0\,, \ldots\,, \quad n.$

1-symbolic dynamics in $N_0 \cup N_1$ is also called *horseshoe*. □

Remark 6.1. Observe that m-symbolic dynamics implies p-symbolic dynamics for any $p \in \mathbb{N}$ such that $m|p$. So, in presence of an horseshoe, p-symbolic dynamics holds for any $p \in \mathbb{N}$. It is also known that a map with a horseshoe is semi-conjugated to a shift $(\sigma_{-1}, \sigma_0, \sigma_1, \ldots) \to (\sigma_{-2}, \sigma_{-1}, \sigma_0, \ldots)$; see, e.g., [22].

In fact, we have the following

Numerical Evidence 6.1. *The map $\mathcal{P}_{\mathcal{H},\Pi^*}$ in (45) has a* 3*-symbolic dynamics. Moreover, an orbit $\{x_j\}_{j=0\ldots,3n}$ corresponding to a given sequence $\sigma_0, \ldots, \sigma_n$, can be chosen to be extendible for $j = 0\ \ldots, 3(n+1)$ and periodic, with period $N \in \{1\,, \ldots\,, 3(n+1)\}$.*

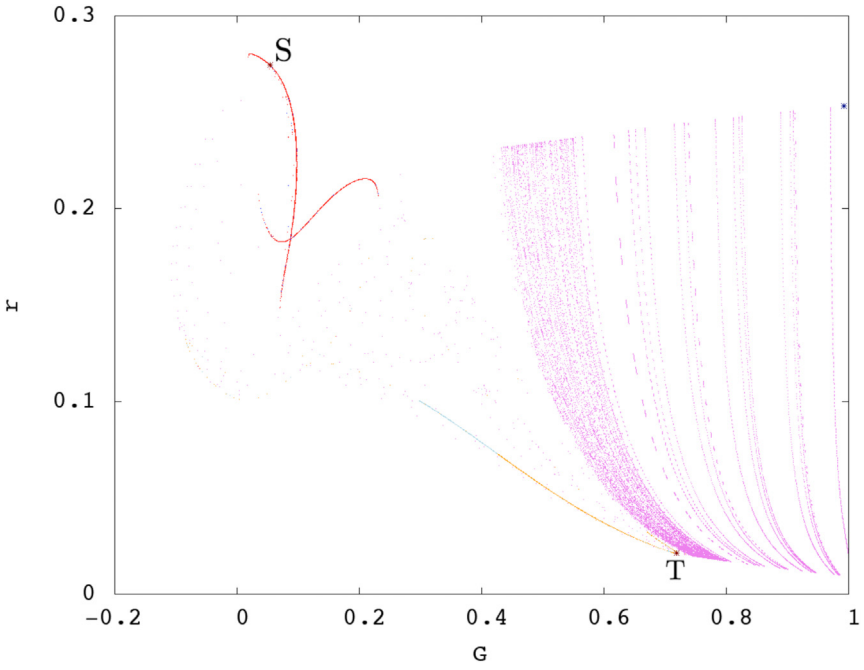

Fig. 23. First return map on the plane $\Pi^\star$; in purple we plot the orbit sections (regular orbits on the right and chaotic see in the left); in blue and red the stable and unstable manifolds of fixed point S; in light-blue and orange the stable and unstable manifolds of fixed point T.

To understand why we assert the Numerical Evidence 6.1, we need to recall, below, the method of *covering relations* developed in [22], and already used in [23] and, recently, in [3] (of course, the interested reader is invited to consult the mentioned literature for more details). It is to be recalled that in [3] the method was used to find an horseshoe, while in this paper we obtain a weaker result (3-symbolic dynamics), seemingly due to the non-existence of heteroclinic connections, as per Numerical Evidence 4.1.

Covering relations and symbolic dynamics

We simplify the material of [22] to the case that the dimension of the space is 2, as this is needed in our application.

Definition 6.2 (*h-Sets, [22,23]*)**.** Let $N \subset \mathbb{R}^2$ be a compact set and let

$$c_N : \mathbb{R}^2 \to \mathbb{R}^2$$

be an homeomorphism such that $c_N(N) = [-1, 1]^2$.

(i) The couple (N, c_N) is called a *h-set*; N is called *support* of the *h*-set.
(ii) Put

$$N_c := [-1, 1]^2\,, \quad N_c^- := \{-1, 1\} \times [-1, 1]\,, \quad N_c^+ := [-1, 1] \times \{-1, 1\}$$

and

$$S(N)_c^l := (-\infty, -1) \times \mathbb{R}\,, \quad S(N)_c^r := (1, \infty) \times \mathbb{R}\,, \quad N_c^{\rm le} = \{-1\} \times [-1, 1]\,, \quad N_c^{\rm ri} = \{1\} \times [-1, 1]$$

The sets

$$N^- = c_N^{-1}(N_c^-)\,, \quad N^+ = c_N^{-1}(N_c^+)\,, \quad N^{\rm le} = c_N^{-1}(N_c^{\rm le})\,, \quad N^{\rm ri} = c_N^{-1}(N_c^{\rm ri})$$

are called, respectively, the *exit set* and the *entry set*, while the sets

$$S(N)^l := c_N^{-1}(S(N)_c^l)\,, \quad S(N)^r = c_N^{-1}(S(N)_c^r)$$

are called, respectively, the *left side*, *right side*, *left edge*, *right edge* of N. □

The following definition is fitted to the special case (realised in our study) that the unstable manifold has dimension 1. The simplification compared to the general definition in [22,23] is based on [22, Theorem 16].

Definition 6.3 (*Covering Relation, [22,23]*)**.** Let $f : \mathbb{R}^2 \to \mathbb{R}^2$ be a continuous map and N and M the supports of two h-sets. We say that M f-covers N and we denote it by $M \overset{f}{\Longrightarrow} N$ if:

(1) $\exists\, q_0 \in [-1, 1]$ such that $f(c_M^{-1}([-1, 1] \times \{q_0\})) \subset \mathrm{int}(S(N)^l \bigcup N \bigcup S(N)^r)$;
(2) $f(M) \bigcap N^+ = \emptyset$;
(3) $f(M^{\mathrm{le}}) \subset S(N)^{\mathrm{l}}$ and $f(M^{\mathrm{ri}}) \subset S(N)^{\mathrm{r}}$ or
(3)' $f(M^{\mathrm{le}}) \subset S(N)^{\mathrm{r}}$ and $f(M^{\mathrm{ri}}) \subset S(N)^{\mathrm{l}}$

If $M = N$, we say that f *self-covers* N.

Conditions (2) and (3) are called, respectively, *exit* and *entry condition*. □

As in [23], we write $A \overset{f}{\Longrightarrow} B \overset{g}{\Longrightarrow} C$, etc, . . ., if $A \overset{f}{\Longrightarrow} B$ and $B \overset{g}{\Longrightarrow} C$, etc.

Theorem 6.4 (*[24]*)**.** *Let N_i, $i = 0, \ldots, k$, be h-sets such that $N_0 = N_k$. Let*

$$f_i : N_{i-1} \to \mathbb{R} \qquad \forall\, i = 1, \ldots, k\,.$$

be a continuous map such that

$$N_0 \overset{f_1}{\Longrightarrow} N_1 \overset{f_2}{\Longrightarrow} \cdots \overset{f_k}{\Longrightarrow} N_k = N_0$$

Then there exists $x_0 \in N_0$ such that

(i) $f_i \circ f_{i-1} \circ \cdots \circ f_1(x_0) \in N_i \quad \forall\, i = 1, \ldots, k$;
(ii) $f_k \circ f_{k-1} \circ \cdots \circ f_1(x_0) = x_0$.

We shall use Theorem 6.4 in the following form.

Corollary 6.1. *Let $D \subset \mathbb{R}^2$*

$$f : \quad D \to \mathbb{R}^2$$

and let N_0, N_1 be h-sets in D. Assume that there exist h-sets $M_i^{(\sigma,\sigma')}$, with $i = 1, \ldots, m-1$ and $\sigma, \sigma' \in \{0, 1\}$, such that

$$N_\sigma \overset{f}{\Longrightarrow} M_1^{(\sigma,\sigma')} \overset{f}{\Longrightarrow} M_2^{(\sigma,\sigma')} \cdots \overset{f}{\Longrightarrow} M_{m-1}^{(\sigma,\sigma')} \overset{f}{\Longrightarrow} N_{\sigma'} \quad \forall\, \sigma\,,\ \sigma' \in \{0, 1\}\,. \tag{46}$$

Then f has m-symbolic dynamics in $N_0 \cup N_1$. In addition, an orbit x_k corresponding, as in Definition 6.1, to a given sequence $\sigma_0, \ldots, \sigma_n$, can be chosen so that it is well defined for $i = 0, \ldots, (n+1)m$ and, moreover, $x_{(n+1)m} = x_0$.

Proof. Let $n \in \mathbb{N}$ and $(\sigma_0, \ldots, \sigma_n)$ a finite sequence of symbols $\sigma_i \in \{0\,,\ 1\}$ having length $n + 1$. Put:

$$\begin{aligned}
&N^0 := N_{\sigma_0} \\
&N^1 := M_1^{(\sigma_0,\sigma_1)}, \quad \ldots \quad N^{m-1} := M_{m-1}^{(\sigma_0,\sigma_1)}, \quad N^m := M_m^{(\sigma_0,\sigma_1)} = N_{\sigma_1} \\
&N^{m+1} := M_1^{(\sigma_1,\sigma_2)} \quad \ldots \quad N^{2m-1} := M_{m-1}^{(\sigma_1,\sigma_2)} \quad N^{2m} := M_m^{(\sigma_1,\sigma_2)} = N_{\sigma_2} \\
&\qquad\qquad \vdots \\
&N^{(n-1)m+1} := M_1^{(\sigma_{n-1},\sigma_n)} \quad \ldots \quad N^{nm-1} := M_{m-1}^{(\sigma_{n-1},\sigma_n)} \quad N^{nm} := M_m^{(\sigma_{n-1},\sigma_n)} = N_{\sigma_n} \\
&N^{nm+1} := M_1^{(\sigma_n,\sigma_0)} \quad \ldots \quad N^{(n+1)m-1} := M_{m-1}^{(\sigma_n,\sigma_0)} \quad N^{(n+1)m} := M_m^{(\sigma_n,\sigma_0)} = N_{\sigma_0}
\end{aligned} \tag{47}$$

By (46), we have

$$N^0 \overset{f}{\Longrightarrow} N^1 \overset{f}{\Longrightarrow} \cdots \overset{f}{\Longrightarrow} N^{(n+1)m}.$$

Moreover, N^0 and $N^{(n+1)m}$ are defined in (47) so as to verify

$$N^0 = N_{\sigma_0} = N^{(n+1)m} \tag{48}$$

(the last row of definitions in (47) has precisely the rôle of making (48) true). Applying Theorem 6.4 with

$$k = (n+1)m\,, \quad f_i = f\,, \quad N_i = N^i \quad \forall\, i = 1, \ldots, (n+1)m\,, \ N_0 := N^0$$

we infer the existence of $x_0 \in N^0 = N_{\sigma_0}$ such that

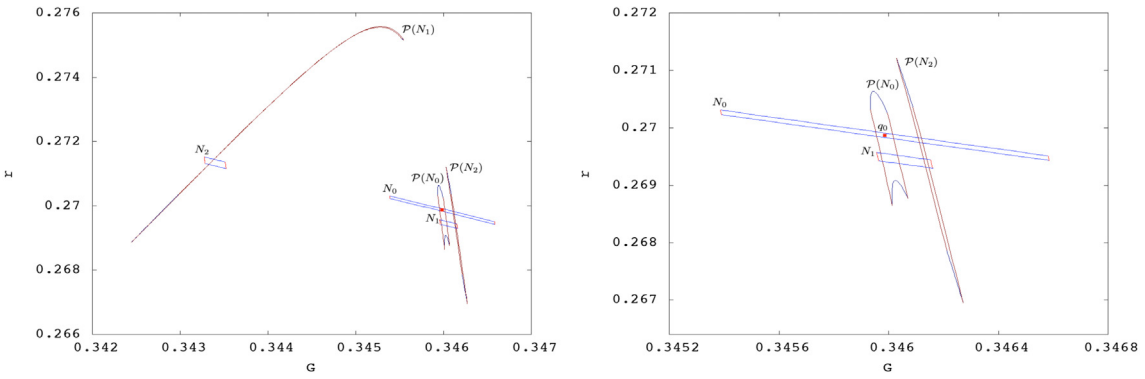

Fig. 24. Numerical Evidence 6.2. Red represents the entry sets and their images and blue the exit sets and their images. The fixed point (r_0, G_0) in (49) is marked in red.

(i) $f^i(x_0) \in N^i \quad \forall\, i = 1, \dots, (n+1)m$;
(ii) $f^{(n+1)m}(x_0) = x_0$.

Taking, in (i), $i = m, 2m, \cdots$, nm, we have the thesis. □

Remark 6.2. As also remarked in [23], if $A \overset{f}{\Longrightarrow} B \overset{f}{\Longrightarrow} C$, not necessarily $A \overset{f^2}{\Longrightarrow} C$. Therefore, under conditions of Corollary 6.1, we cannot conclude that f^k has an horseshoe.

Symbolic dynamics for $\mathcal{P}_{\mathcal{H},\Pi^*}$

Let us consider the map $\mathcal{P}_{\mathcal{H},\Pi^*}$ in (45). The stable and unstable eigenvectors related to $D\mathcal{P}_{\mathcal{H},\Pi^*}$ at

$$q_0 = (r_0, G_0) = (0.26987, 0.345986) \tag{49}$$

have directions, respectively,

$$v^s = (-0.556268\,,\ 0.831003)\,, \quad v^u = (-0.998774\,,\ 0.0495113),$$

and the angle between them is $\alpha = 0.296467\,\pi$. Observe that q_0 is the projection of the point (44) on the plane (r, G). We denote as N_0 the parallelogram through q_0 with edges parallel to v^s and v^u, namely:

$$N_0 = q_0 + A_0 v^s + B_0 v^u\,, \tag{50}$$

where A_0, B_0 are the real intervals

$$A_0 = [-0.000719075, 0.000719075]\,, \qquad B_0 = [-0.0000400491, 0.0000400491]\,.$$

We define two analogous parallelograms:

$$N_1 = q_1 + A_1 \widetilde{v}^s + B_1 v^u\,, \qquad N_2 = q_2 + A_2 v^s + B_2 v^u \tag{51}$$

where

$$\begin{cases} q_1 = (r_1, G_1) = (0.269552, 0.34598) \\ q_2 = (r_2, G_2) = (0.27124, 0.343432) \end{cases},$$

with

$$A_1 = [-0.000028763, 0.000208532]\,, \qquad B_1 = [-0.000144177, 0.00000400491]\,,$$

$$A_2 = [-0.000179769, 0.000107861]\,, \qquad B_2 = [-0.00000400491, 0.000200246]$$

and

$$\widetilde{v}^s = (-0.556143, 0.831003)\,.$$

Then we have the following (see Fig. 24)

Numerical Evidence 6.2.

$$N_0 \overset{\mathcal{P}_{\mathcal{H},\Pi^*}}{\Longrightarrow} N_0 \overset{\mathcal{P}_{\mathcal{H},\Pi^*}}{\Longrightarrow} N_1 \overset{\mathcal{P}_{\mathcal{H},\Pi^*}}{\Longrightarrow} N_2 \overset{\mathcal{P}_{\mathcal{H},\Pi^*}}{\Longrightarrow} N_0 \quad , \quad N_2 \overset{\mathcal{P}_{\mathcal{H},\Pi^*}}{\Longrightarrow} N_1\,.$$

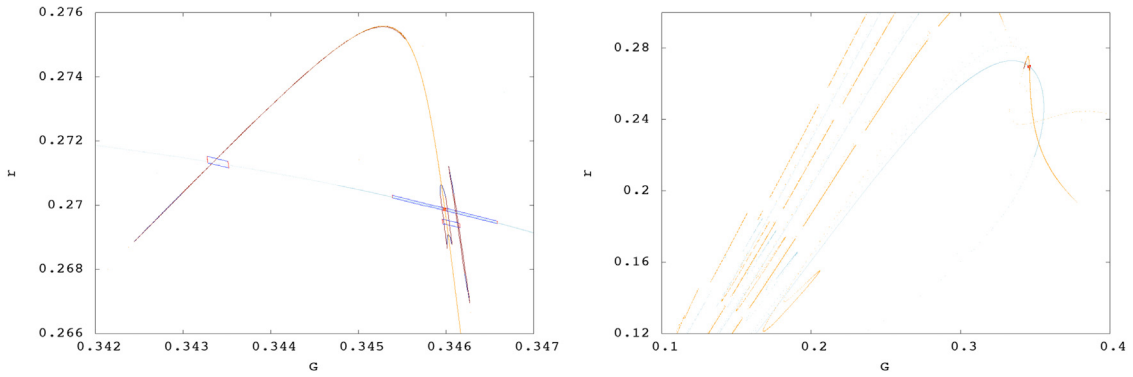

Fig. 25. Details on the construction of the sets (50) and (51). Light blue and orange denote, respectively, the stable and unstable manifolds. The right figure represents a wider region.

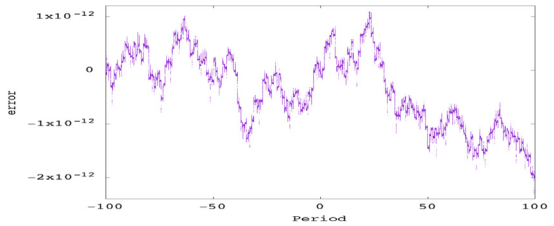

Fig. 26. Relative energy error in the propagation of the periodic orbit Γ_s versus number of its period T_s.

Splitting such relations as

$$\begin{cases} N_0 \overset{\mathcal{P}_{\mathcal{H},\Pi^*}}{\Longrightarrow} N_1 \overset{\mathcal{P}_{\mathcal{H},\Pi^*}}{\Longrightarrow} N_2 \overset{\mathcal{P}_{\mathcal{H},\Pi^*}}{\Longrightarrow} N_0 \\ N_0 \overset{\mathcal{P}_{\mathcal{H},\Pi^*}}{\Longrightarrow} N_1 \overset{\mathcal{P}_{\mathcal{H},\Pi^*}}{\Longrightarrow} N_2 \overset{\mathcal{P}_{\mathcal{H},\Pi^*}}{\Longrightarrow} N_1 \\ N_1 \overset{\mathcal{P}_{\mathcal{H},\Pi^*}}{\Longrightarrow} N_2 \overset{\mathcal{P}_{\mathcal{H},\Pi^*}}{\Longrightarrow} N_0 \overset{\mathcal{P}_{\mathcal{H},\Pi^*}}{\Longrightarrow} N_0 \\ N_1 \overset{\mathcal{P}_{\mathcal{H},\Pi^*}}{\Longrightarrow} N_2 \overset{\mathcal{P}_{\mathcal{H},\Pi^*}}{\Longrightarrow} N_0 \overset{\mathcal{P}_{\mathcal{H},\Pi^*}}{\Longrightarrow} N_1 \end{cases}$$

and in view of Corollary 6.1, the Numerical Evidence 6.1 follows, with N_0, N_1, N_2 as in (50), (51).

We conclude this section providing some detail on the construction of the sets (50) and (51). As highlighted in Fig. 25, such sets are obtained inspecting the homoclinic intersections of the stable and unstable manifolds through q_0.

7. Control of errors and conclusions

In this section we describe how we controlled numerical errors and draw some conclusions.

In our computations, we used a double precision. One check of errors was performed by the control of energy which, being a first integral of motion should be constant. Its relative variation was required not to exceed 10^{-10}, but the error we obtain in our simulations is much smaller. For the orbits we deal with in Section 4, 5, 6 the relative error is comparable, so we choose to show orbit Γ_s. In Fig. 26, it can be seen that the relative error remains less that $2.5 \cdot 10^{-12}$ in 200 iterations of the map (38).

As a further test, we performed onward and backward integrations of orbits of the map (38) starting with different initial conditions; as example cases, we show 4 orbits with the following initial conditions:

$$\begin{cases} \mathrm{R} = -11.3668\,, \quad \mathrm{G} = 0.992515\,, \quad \mathrm{r} = 0.13165\,, \quad \mathrm{g} = 0.878179\,\pi \quad \text{(blue)} \\ \mathrm{R} = -10.6704\,, \quad \mathrm{G} = 0.8\,, \quad \mathrm{r} = 0.13165\,, \quad \mathrm{g} = \pi \quad \text{(light} - \text{blue)} \\ \mathrm{R} = -9.07533\,, \quad \mathrm{G} = 0.5\,, \quad \mathrm{r} = 0.13165\,, \quad \mathrm{g} = \pi \quad \text{(green)} \\ \mathrm{R} = -8.94348\,, \quad \mathrm{G} = 0.48\,, \quad \mathrm{r} = 0.13165\,, \quad \mathrm{g} = \pi \quad \text{(red)} \end{cases} \tag{52}$$

In Fig. 27, we plot the sections map (38) of the 4 orbits with initial conditions (52). In Fig. 28, we show the errors performed after a number of iterations onward and backward of the map (38); the 4 panels show the errors of the 4

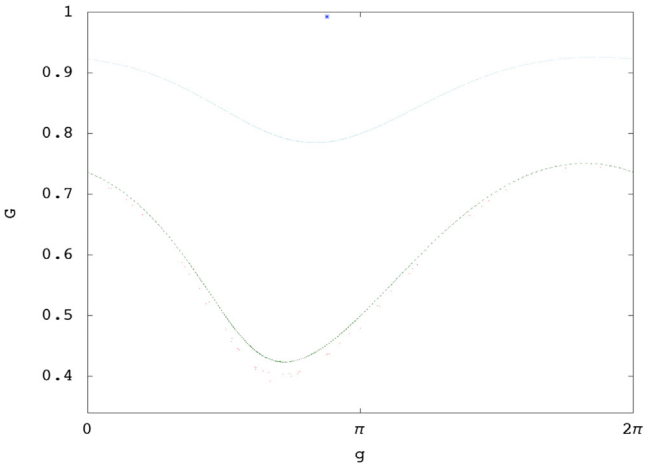

Fig. 27. Sections of map (38) of the 4 orbits starting with initial conditions (52).

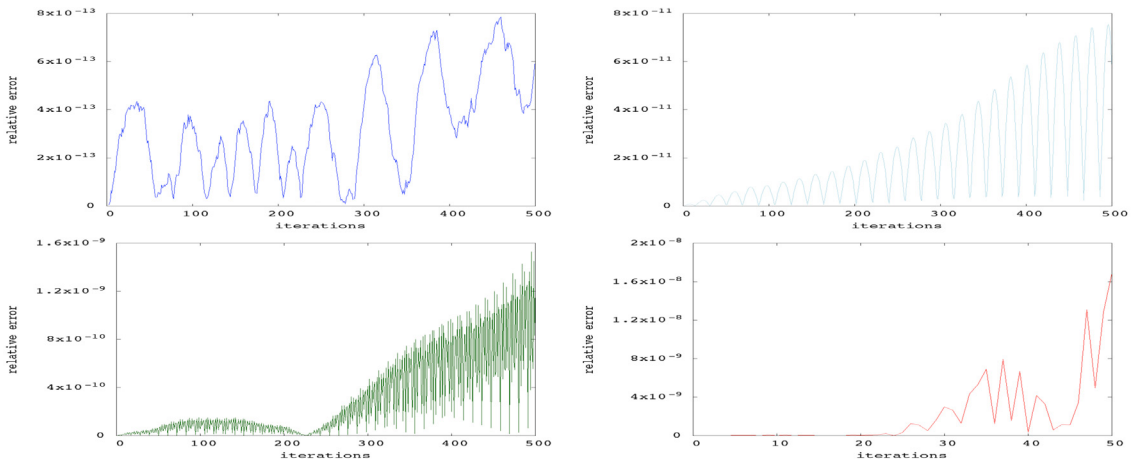

Fig. 28. Onward and backwards integration of orbits of map (38) starting with initial conditions (52) (respectively, blue, light-blue, green and red): relative errors of the coordinates (G, g) of the onward and backward integrations versus the number of iteration of the map are plotted.

orbits (respectively with the same colours) versus the number of iterations of the map (38). The number of iterations (500) is chosen as a reference because our simulations do not exceed this number.

We are now ready for the conclusions.

In this paper, we discussed about the effects of the level sets of the function (16) on the dynamics of the Hamiltonian (10). Specifically, in a range where the energy of the averaged, reduced 2-degrees of freedom system (10) has three different scales, one expects that the motions of the system obey to Conjectures 1.1 and 1.3. In particular, due to the non-integrability of the system, chaos is expected closely to the envelope $\mathcal{M}_0$ in (21) of the separatrices of E. After fixing the energy level (33), we computed a Poincaré map (38), which showed the existence of only two fixed points, having elliptic, hyperbolic character. The level sets of E turn to vary a little along the orbit Γ_s generated by the elliptic fixed point, while it varies more along the orbit Γ_u generated by the hyperbolic fixed point. However, it turns out that Γ_u spends most of its time close to the saddle of $\mathcal{M}_0$, and we investigated the phase space around Γ_u. We used various 2-dimensional first return maps, and we found a homoclinic tangency using one of them; some heteroclinic intersection using another one. Applying the analysis developed in [22–24], we found 3-symbolic dynamics in the sense of Definition 6.1. Our results are so in complete agreement with Conjecture 1.3, while, as remarked in the introduction, Conjecture 1.2 is still open.

CRediT authorship contribution statement

Sara Di Ruzza: Methodology, Software, Validation, Formal analysis, Investigation, Data curation, Writing – original draft, Writing – review & editing, Visualisation. **Gabriella Pinzari:** Conceptualisation, Methodology, Formal analysis, Investigation, Data curation, Writing – original draft, Writing – review & editing, Visualisation, Supervision, Project administration, Funding acquisition.

Declaration of competing interest

The authors declare that they have no known competing financial interests or personal relationships that could have appeared to influence the work reported in this paper.

Acknowledgements

We thank the anonymous reviewers for their stimulating remarks, which helped to improve the presentation of the results in the paper. This paper is supported by the ERC project 677793 Stable and Chaotic Motions in the Planetary Problem (2016–2022). Figs. 2–4 have been produced with Mathematica®. Fig. 1 has been produced with Vectornator and Figs. 5–28 have been produced with Gnuplot.

References

[1] Arnold VI. Small denominators and problems of stability of motion in classical and celestial mechanics. Russian Math Surv 1963;18(6):85–191.
[2] Pinzari G. A first integral to the partially averaged newtonian potential of the three-body problem. Celestial Mech Dynam Astronom 2019;131(5):22.
[3] Di Ruzza S, Daquin J, Pinzari G. Symbolic dynamics in a binary asteroid system. Commun Nonlinear Sci Numer Simul 2020;91(16):105414.
[4] Pinzari G. Perihelion librations in the secular three-body problem. J Nonlinear Sci 2020;30(4):1771–808.
[5] Pinzari G. Euler integral and perihelion librations. Discrete Contin Dynam Syst - A 2020.
[6] Giorgilli A. Appunti di meccanica celeste. 2008, http://www.mat.unimi.it/users/antonio/meccel/Meccel_5.pdf.
[7] Chierchia L, Pinzari G. The planetary *N*-body problem: symplectic foliation, reductions and invariant Tori. Invent Math 2011;186(1):1–77.
[8] Laskar J, Robutel P. Stability of the planetary three-body problem. I. Expansion of the planetary Hamiltonian. Celestial Mech Dynam Astronom 1995;62(3):193–217.
[9] Féjoz J. Démonstration du 'théorème d'Arnold' sur la stabilité du système planétaire (d'après Herman). Ergodic Theory Dynam. Systems 2004;24(5):1521–82.
[10] Pinzari G. On the kolmogorov set for many–body problems [Ph.D. thesis], Università Roma Tre; 2009.
[11] Chierchia L, Pinzari G. Planetary Birkhoff normal forms. J Mod Dyn 2011;5(4):623–64.
[12] Chen Q, Pinzari G. Exponential stability of fast driven systems, with an application to celestial mechanics. Nonlinear Anal 2021;208:112306.
[13] Delshams A, Kaloshin V, de la Rosa A, Seara TM. Global instability in the restricted planar elliptic three body problem. Comm Math Phys 2019;366(3):1173–228.
[14] Guardia M, Martín P, Seara TM. Oscillatory motions for the restricted planar circular three body problem. Invent Math 2016;203(2):417–92.
[15] Bolotin S. Symbolic dynamics of almost collision orbits and skew products of symplectic maps. Nonlinearity 2006;19(9):2041–63.
[16] Féjoz J, Guardia M. Secular instability in the three-body problem. Arch Ration Mech Anal 2016;221(1):335–62.
[17] Fejoz J, Guardia M, Kaloshin V, Roldan P. Kirkwood gaps and diffusion along mean motion resonances in the restricted planar three body problem. J Eur Math Soc 2014.
[18] Guardia M, Kaloshin V, Zhang J. Asymptotic density of collision orbits in the restricted circular planar 3 body problem. Arch Ration Mech Anal 2019;233(2):799–836.
[19] Delshams A, de la Llave R, Seara TM. Geometric properties of the scattering map of a normally hyperbolic invariant manifold. Adv Math 2008;217(3):1096–153.
[20] Lega E, Guzzo M, Froeschlé C. Theory and applications of the fast Lyapunov indicator (fli) method. In: Chaos detection and predictability. Springer; 2016, p. 35–54.
[21] Delshams A, de la Llave R, Seara TM. A geometric approach to the existence of orbits with unbounded energy in generic periodic perturbations by a potential of generic geodesic flows of $\mathbf{T}^2$. Comm Math Phys 2000;209(2):353–92.
[22] Zgliczynski P, Gidea M. Covering relations for multidimensional dynamical systems. J Differential Equations 2004;202(1):32–58.
[23] Gierzkiewicz A, Zgliczyński P. A computer-assisted proof of symbolic dynamics in hyperion's rotation. Celestial Mech Dynam Astronom 2019;131(7):33.
[24] Wilczak D, Zgliczynski P. Heteroclinic connections between periodic orbits in planar restricted circular three-body problem – a computer assisted proof. Comm Math Phys 2003;234(1):37–75.